3-21-2017

Heat Flux Modeling of Asymmetrically Heated and Cooled Thermal Stimuli

Matthew Hardy
University of South Florida, mhardy1@mail.usf.edu

Heat Flux Modeling of Asymmetrically Heated and Cooled Thermal Stimuli

by

Matthew Hardy

A thesis submitted in partial fulfillment
of the requirements for the degree of
Master of Science in Mechanical Engineering
Department of Mechanical Engineering
College of Engineering
University of South Florida

Co-Major Professor: Kyle B. Reed, Ph.D.
Co-Major Professor: Rasim Guldiken, Ph.D.
Nathan Crane, Ph.D.

Date of Approval:
March 6, 2017

Keywords: Thermal Perception, Computer Simulation, Finite Element Model, Haptics, Thermal Comfort

Acknowledgments

I would like to express my extreme gratitude to my co-major advisors, Dr. Kyle B. Reed and Dr. Rasim Guldiken. Their knowledge, creativity and experience has served to inspire and guide me throughout the course of my research and beyond. Also, for taking time out of their schedules every week to meet with me and keep me focused and on track. I would also like to thank my committee member, Dr. Nathan Crane, for agreeing to serve and critique this work.

I would like to thank my lab mates Ben, Tyagi, Christina, Mehdi, Fatemeh and Milli for engaging in thoughtful and civilized discussion as well as helping me with different aspects of my research, even though they were busy themselves. Additionally, I would like to thank Dr. Ahmad Manasrah and Dr. Emre Tufekcioglu for guidance at the outset of myresearch.

Finally, I would like to thank my family. My mother and father have supported and encouraged me throughout my life even when I was most undeserving of it. I would like to thank my brothers, Kyle and Scott, for putting up with me even though I was not always a particularly good older brother.

This material is based upon work supported by the National Science Foundation under Grant Number IIS-1526475.

Table of Contents

List of Tables iii

List of Figures iv

Abstract vii

Chapter 1: Introduction 1

Chapter 2: Background 4
2.1 Heat Flux 4
2.2 Simulated Models 7
2.2.1 Types of Simulations 8
2.2.2 Simulation Quality Criteria 9
2.3 Thermal Haptics 12

Chapter 3: Heat Flux Associated with Heating and Cooling Cycles 16
3.1 Heat Flux: A Theoretical Analysis 16
3.1.1 Analytic Solution to the Heat Equation 17
3.1.2 Isolated Heating and Cooling Segments 18
3.1.2.1 Heating From Skin Temperature 19
3.1.2.2 Heating From Below Skin Temperature 20
3.1.2.3 Cooling From Above Skin Temperature 20
3.1.2.4 Cooling From Skin Temperature 21
3.2 Simulated Haptic Model 22
3.2.1 Solidworks Model 23
3.2.2 ANSYS Transient Thermal Setup 26
3.2.2.1 Simulation Parameters 30
3.2.2.2 Nodal Convergence Study 32
3.2.2.3 Initial and Boundary Conditions 35
3.3 Heat Flux: A Simulated Analysis 36
3.3.1 ANSYS Numerical Method of Solving the Heat Equation 36
3.3.2 Isolated Heating and Cooling Segments 38
3.3.2.1 Heating From Skin Temperature 39
3.3.2.2 Heating From Below Skin Temperature 40
3.3.2.3 Cooling From Above Skin Temperature 41
3.3.2.4 Cooling From Skin Temperature 42
3.4 Asymmetric Heating and Cooling Cycles 42

3.4.1 Temporal Patterns and Spatial Patterns 44
3.4.1.1 Horizontal 45
3.4.1.2 Diagonal 47
3.4.1.3 Arbitrary 48
3.4.1.4 Simulated Patterns 49
3.4.2 Heat Flux Profile for Two Actuators 49
3.4.3 Heat Flux Profile for Four Actuators 58
3.5 Proposed Correlation Between Experiment and Simulation 62
3.5.1 Perception Metrics 66
3.5.2 Correlation with Heat Flux 68
3.6 Optimizing Heating and Cooling Patterns 70
3.6.1 Overlapping Time Patterns 70
3.6.2 Rearranged Heating and Cooling Patterns 73
3.6.3 Non-Linear Time Patterns 74
3.6.4 Efficiency of Optimized Patterns 75

Chapter 4: Conclusion and Future Work 79

List of References 81

Appendices 85
Appendix A: IEEE Copyright Permission 86
Appendix B: Element Quality Metrics for Cylinder 87

List of Tables

Table 3.1 Thermal properties of human skin and polyurethane rubber 23

Table 3.2 Dimensions used for model creation 24

Table 3.3 Nodal convergence metrics 33

Table 3.4 Heat flux difference values for the horizontal pattern 51

Table 3.5 Heat flux difference values for the diagonal pattern 54

Table 3.6 Heat flux difference values for the arbitrary pattern 56

Table 3.7 ASHRAE thermal comfort scale 63

List of Figures

Figure 3.1 Four isolated heating and cooling segments 19

Figure 3.2 Analytic case 1 using Fouriers equation to calculate the heat flux profile for the scenario where the temperature increases one degree from skin temperature over 30 seconds 19

Figure 3.3 Analytic case 2 using Fouriers equation to calculate the heat flux profile for the scenario where the temperature increases one degree from below skin temperature over 30 seconds 20

Figure 3.4 Analytic case 3 using Fouriers equation to calculate the heat flux profile for the scenario where the temperature decreases one degree from above skin temperature over ten seconds 21

Figure 3.5 Analytic case 4 using Fouriers equation to calculate the heat flux profile for the scenario where the temperature decreases one degree from skin temperature over ten seconds 22

Figure 3.6 Cross-sectional view showing the dimensions for the cylinder 24

Figure 3.7 Chord length and arc length used to create the actuator cross section 25

Figure 3.8 Angle offset of actuators relative to the centerline of actuators 26

Figure 3.9 ANSYS transient thermal setup screen 27

Figure 3.10 ANSYS material selection 28

Figure 3.11 Geometry setup in ANSYS design modeler 29

Figure 3.12 ANSYS simulation tree outline 30

Figure 3.13 Probe locations for nodal convergence study 33

Figure 3.14 A graphical representation of the heat flux values generated for a series of mesh sizes 34

Figure 3.15 1mm mesh generated on cylinder 34

Figure 3.16 Heat flux produced when temperature is applied to body vs. face 36

Figure 3.17 Simulated case 1 where the temperature increases one degree over thirty second from 32˚C to 33˚C 39

Figure 3.18 Simulated case 2 where the temperature increases one degree over thirty second from 31.5˚C to 32.5˚C 40

Figure 3.19 Simulated case 3 where the temperature decreases one degree over ten second from 32.5˚C to 31.5˚C 41

Figure 3.20 Simulated case 4 where the temperature decreases one degree over ten second from 32˚C to 31˚C 42

Figure 3.21 Global coordinate system orientation and actuator names 43

Figure 3.22 One cycle of 30/10 heating and cooling cycle 46

Figure 3.23 The horizontal heating pattern 46

Figure 3.24 The diagonal heating pattern 47

Figure 3.25 The arbitrary heating pattern 48

Figure 3.26 Probe locations under and between first two actuators 50

Figure 3.27 Heat flux profile for horizontal simulation patterns 53

Figure 3.28 Heat flux profile for diagonal simulation patterns 55

Figure 3.29 Heat flux profile for arbitrary simulation patterns 57

Figure 3.30 Probe locations for four actuator study 59

Figure 3.31 Heat flux profile for the three spatial patterns at the 30/10 heating and cooling rate 61

Figure 3.32 Temporal pattern thermal sensation metrics 63

Figure 3.33 Spatial pattern thermal sensation metrics 64

Figure 3.34 Combined temporal and spatial pattern metrics 67

Figure 3.35 Absolute maximum heat flux difference for probes in the simulation 68

Figure 3.36 Mathematical relationship between thermal sensation and heat flux 69

Figure 3.37 Incorrect overlapping temporal pattern 71

Figure 3.38 Proper overlapping temporal pattern 72

Figure 3.39 Comparison of horizontal and horizontal rearranged 73

Figure 3.40 The 30/10 non-linear heating and cooling pattern 75

Figure B.1 Mesh quality on area of interest 87

Figure B.2 Aspect ratio on area of interest 88

Figure B.3 Skewness on area of interest 89

Abstract

Thermal sensation is one of the most dynamic stimulus-response systems in the human body. It is relied upon for safety, comfort and general equilibrium of the human body. Thermal sensation is dependent upon many variables such as area of effected skin, rate of temperature change and location of stimulation. It has been shown that certain rates of change can intensify the sensation of heating or cooling. Conversely, sufficiently low rates of change can go undetected by the skin. As such, the thermal response system can be manipulated by the proper combination of applied hot and cold stimuli. Previous research has shown that through precise application of an asymmetrically heated and cooled thermal display, a sensation of constant cooling can be perceived. This thesis seeks to (1) explore the heat flux characteristics of the thermal display through the use of computer simulations, (2) test a hypothesis about the relationship between thermal sensation and heat flux and (3) examine modifications of the thermal display patterns with the intention of producing more intense thermal sensations.

To characterize the heat flux patterns produced by the thermal display, finite element simulations, performed using commercially available software ANSYS©. Simulations are conducted on individual heating and cooling rates to examine the expected values of heat flux as temperatures approach and diverge from skin temperature. Evaluated in the cylindrical coordinate system (axial, angular and radial), the simulations showed a slight nonlinear heat flux generation at the beginning of heating and cooling, but after the initial transient period, this gave way to a strong linear generation of increasing or decreasing heat flux.

Simulations were performed that represent the physical experiments implemented in previous research. These simulations were done in two parts: the first examines a small subregion with finer detail on the area between heating and cooling stimuli, the second is a larger scale

examination of the heat flux profile of the thermal display. Initially it was observed that directly under the thermal stimulus, in the radial direction, the heat flux was almost perfectly in-phase with the oscillation of temperature whereas between the stimuli, it was nearly 180 degrees out of phase. The heat flux in the axial and angular directions under the thermal stimulus were negligible. Additionally, between stimuli, the values were nearly 180 degrees out of phase with temperature. Additionally, it was observed that the heat flux profiles for all patterns used in the thermal display were approximately identical.

From the data gathered by the simulations in conjunction with the thermal sensation data from previous research, a linear relationship is hypothesized that relates these two quantities. This relationship was then used to determine the theoretical thermal sensations of newly developed thermal display patterns in order to determine which are best suited for future physical experimentation.

Chapter 1: Introduction

The human body relies on numerous systems of stimulus and response within its environment and physiology for safety and comfort. Taste gives the body a strong sense of whether or not something is safe to ingest. Sight allows us to avoid unsafe situations and locations. Smell gives us the ability to identify both unpleasant and beautiful objects. These senses also allow us to detect subtle cues given off by others around us. Many of our natural senses can be used independently or in conjunction with each other. Material properties such as texture and temperature can be identified without the use of sight. Sound is independent of all other senses. The ability to taste is made much less effective without the use of smell. All of the sensory responses are the result of external stimuli that interact with sensory receptors that are located throughout the body. The sensory receptors detect external changes in the environment and transmit signals to the brain. The brain interprets these signals and responds accordingly. Well known receptors include: chemoreceptors, mechanoreceptor and thermoreceptors. Each of these is responsible for specific interactions with the environment. Chemoreceptors and mechanoreceptor are responsible for senses such as taste, smell and touch [1, 2]. Thermoreceptors are responsible for temperature sensation as well as the control and regulation of body temperature [3].

It is through the exploitation of the thermoreceptor response characteristics that this thesis is based. Kenshalo [4, 5] showed that the rate of temperature change determines the perceivable thermal threshold. Additionally, thermoreceptors respond to decreasing temperatures much quicker than increasing temperatures [6, 7]. It is through this principle that the method for generating a perceived sense of constant cooling emerged. Manasrah et al. [8] showed that a perceived sense of constant cooling could be achieved through the use of asymmetrically heated and cooling thermal actuators. Controlling the rate of temperature change, heating below the threshold and cooling

above the rate for perception, constant cooling was felt by a majority of the subjects. However, thermal perception is not based on absolute temperature but by temperature difference or heat flux. Therefore, the primary contribution of this thesis is the development of a relationship between between the thermal perception of the patterns used in the physical experiment and the heat flux values calculated from the simulations.

Chapter two provides a foundation for the various aspects of this thesis. First, the concept of heat flux is explained. A brief history of the natural phenomenon, which has arisen from a large body of empirical evidence instead of derived from first principles is given. Because of this, heat flux can be somewhat difficult to comprehend from a physical standpoint. Examples are given with the intention of making this abstract concept more clear. Following this, the usefulness of computer models and simulations are explained. The use of computer models in science and industry has become an everyday tool. The wide range of scientific fields that can exploit the benefits of simulations are also listed. Next, the concept of thermal haptics is explained with a specific emphasis on how it pertains to this study. The primary purpose of this thesis is based of the principles of thermal haptics and how it was utilized in previous works. The chapter concludes with a recapitulation on the work for which this thesis is based.

Chapter three serves as the primary work done in the search to understand and define the relationship between the thermal haptic device developed and the thermal sensation achieved in previous work. The first section provides an analytic evaluation of the different heating and cooling cycles used from the physical experiment. This section also serves to verify the simulations performed. Section two explains the modeling component of the simulation. This provides details on the accuracy of the model relative to the experimental setup. Additionally, the simulation setup and parameters used to accurately recreate the actual setup are explained. Metrics and evaluations of the model and simulation that ensure the validity of the results are the final component of section two. Section three explains the methods used by ANSYS to evaluate the different simulations performed through out this study. The individual heating and cooling segments are then simulated

and compared with the analytic evaluations in order to verify the subsequent simulated asymmetric heating and cooling patterns.

The asymmetric heating and cooling cycles used to create a perceived sense of constant cooling are the focus of the second half of chapter three. The heating and cooling patterns used in the physical experiment are simulated and examined. The heat flow characteristics of nine spatial and timing patterns are detailed. Following this, a correlation between the heat flux profile of each pattern and actual thermal sensation is developed. This relationship will then used to determine the potential magnitude of thermal sensation of the new patterns developed. The final section of chapter three defines new patterns. These patterns are simulated and their heat flux characteristics are used to determine their effectiveness in achieving the sense of constant cooling. All simulations done were evaluated using the cylindrical coordinate system. However, Cartesian coordinates are used interchangeably throughout this thesis. The angular dimension is identical to the x-direction, the radial dimension is identical to the y-direction, and the axial dimension is identical to the z-direction.

Chapter four concludes the work done in this thesis. The effectiveness of asymmetric heating and cooling patterns are summarized and recommendations are given with the intention of increasing the sensation of constant cooling. Additional experiments are suggested to further explore the relationship between heat flux and thermal perception.

Chapter 2: Background

The contents of this thesis are a combination of several disciplines in engineering. A fundamental explanation of each topic is given. The final section explains how the topics relate in the context of previous work done.

2.1 Heat Flux

Joseph Fourier is credited with first developing the mathematics behind the mode of heat transfer known as heat flux in his "Analytic Theory of Heat" [9]. Fourier made the following statement on the development of heat conduction: "Primary causes are unknown to us; but are subject to simple and constant laws, which may be discovered by observation" [9]. In short, the principle of heat flux is derived from a multitude of observations instead of a mathematical proof.

Heat flux is defined as the rate of heat transfer per unit area, e.g., W/m^2. Heat energy is conducted through a medium based on its material properties and it is often useful to view this on a per unit area basis. However, to have a better understanding of this definition, we need to know what the driving force is behind this process. The equation for heat flux is

$$q''_n = -k * \frac{dT}{dm} \tag{2.1}$$

where q''_n is the heat flux per unit area in the direction normal to the surface through which heat is being conducted, k is the thermal conductivity unique to the material and $\frac{dT}{dm}$ is the directional temperature gradient, where m represents either x, y or z, within the object of interest. From Equation 2.1, it is seen that the heat flux through an object is proportional to the conduction coefficient specific to the material. These types of laws are known as nondeterministic because they

rely on specific knowledge of the system and are not general statements that apply to all cases [10]. Additionally, on a macroscopic scale, it becomes apparent that the driving force behind heat flux is the temperature gradient within an object. The temperature gradient is a function of the initial temperature of the object and the boundary temperatures of the object, due either to an applied temperature, convecting fluid or other generation source. The set of temperatures to be observed are directly related to the molecular energy of the medium; higher temperatures are associated with higher molecular energy and therefore a higher rate of collision between atoms. The collision between atoms results in a transfer of momentum between them, and gradually increases the energy associated with the cooler end of the temperature gradient thereby increasing its temperature. It is for this reason that heat flows from higher temperatures to lower temperatures and necessitates the negative sign to define this flow of heat as positive.

Developing the temperature profile inside an object is the first step in calculating the heat flux through an object. A series of techniques have been developed to evaluate the temperature profile of an object. For example separation of variables generates an exact solution for the temperature profile. Duhamels theorem develops an approximate solution for problems involving time dependent boundary conditions, and nodal analysis can calculate temperature values at discrete locations in an object [10]. The initial conditions and boundary conditions of a particular system determine its unique temperature profile. The profile can be a function of space and/or time; increasing the number of variables increases the complexity and time to generate a solution. Once the temperature profile is known, a series of additional quantities can be calculated.

Heat flux is driven by the temperature gradient of an object. However, certain objects can feel colder than others even if both are at an identical temperature. This phenomenon is due to the thermal conductivity of a material, k with units W/m*K. In solid substances, heat is conducted through the vibration of the lattice structure of the material, creating structural waves known as phonons [11]. It is apparent from this definition that the conductivity of a material is susceptible to change based on external influences such as pressure and temperature. The thermal conductivity of materials such as iron, copper and silver decrease linearly with an increase in pressure due to lattice

distortion. However, the lattice of materials like lead, tin and zinc become more organized with increasing pressure and therefore exhibit an increase in thermal conductivity [12]. It can be inferred that having a more organized atomic lattice leads to a higher thermal conductivity. Similarly, an increase in temperature will decrease the thermal conductivity of an object [13]. As vibration among atoms in a material is increased (caused by an increase in temperature), so too is the disorder of the atomic structure. This decreases the molecular momentum of phonon waves generated by a heating source thereby decreasing a material's ability to transfer heat. The importance of a material's molecular lattice structure in transferring heat is illustrated by recognizing that at an identical temperature below skin temperature, aluminum will feel cooler than wood.

Conductive heat flux is the method by which heat energy is propagated through a solid. This phenomenon is independent of direction. Equation 2.1 was developed through experimental observation but it can be used in conjunction with conservation of energy to fully understand the heat flow characteristics of a control volume. The heat energy flowing into the system is compared to the heat energy leaving the system and the difference is the amount of energy stored in the system. This allows for the creation of a transient model of the heat flow equation.

$$\nabla(k\nabla T) + g = \rho c \frac{dT}{dt} \tag{2.2}$$

where, ∇ is the Laplacian operator, k, ρ and c are thermal conductivity, density and specific heat capacity respectively, and g is internal energy generation. It is from this equation that the heat flow characteristics of the system presented in this thesis are derived. Even with some simplifying assumptions, such as eliminating the internal generation term, this equation is too laborious and time consuming to develop solutions for the number of unique systems involved. This is what necessitates the need for computer simulation software.

Equation 2.2 can be simplified for analysis in any of the three coordinate directions and time. This is often done due to the arduous nature of the solution process. However, this simplified version of the solution produces only a partial description of the heat flow pattern of a system. It is

often desirable or necessary to understand the complete heat flow characteristics of a system. The use of simulated models easily allows for a solution in all three coordinate directions. Furthermore, the directional heat flux can be combined to calculate the resultant magnitude, or "total" value, of heat flux. Through out the course of this thesis, it will be shown that all four of these heat flux values, x, y, z and total (angular, radial, axial and total) are uniquely useful and help to describe different aspects of the heat flow characteristics.

2.2 Simulated Models

Computer models have played a major roll in science and engineering since shortly after World War II. Like much of the science and technology of today, computer simulation has its roots in military research and development. Simulation tools were quickly expanded toward other areas such as education and industry. These tools are used for many reasons including solving systems that are too complicated to be solved analytically or to gain a better understanding of data that already exists. Many of the governing equations of nature are complicated partial differential equation. The one-dimensional case of many of these equations is easily solved, however, two- and three-dimensional analysis can be either very time consuming or even impossible. Simulations give us insight into natural systems without having to expend a lot of capital in a physical setup that may ultimately prove a failure. In addition to scientific models, simulations can also be used to explore social models such as population growth and the spread of disease. Computer simulations are an invaluable tool, if performed correctly. Many aspects of a simulation setup must be created properly, within an acceptable range, in order to obtain appropriate results. It is easy for the output of a simulation to diverge if, for example, the mesh quality is poor or the time-stepping is inadequate. Engineering professionals have been working for decades to develop more accurate methods for solving computer simulations.

The underlying method behind solving a simulation is to divide the object under examination in to a discrete set of nodes and apply the equations that govern the physical phenomenon. The nodes are generated through a meshing process. The user specifies the type and size of the

mesh and then the software creates the mesh accordingly. Meshs can range from coarse to very fine. Generally, an object will have a range of mesh sizing with areas of interest having much finer mesh sizing and peripheral areas having a more coarse mesh. The mesh must comply with certain metrics such as quality, skewness and aspect ratio that ensure the quality of the solution. Once the mesh is created and verified, governing equations are applied in a finite difference or finite element method. Specific quantities are calculated at each node, based on initial conditions and boundary conditions, and subsequent data is gathered. In the context of this thesis, the temperature at each node is calculated and the heat flux data is extrapolated.

2.2.1 Types of Simulations

A variety of simulation methods exist that are used to study both scientific and social models. Topics ranging from structural, fluid and thermal experiments to the spread of disease, population expansion and even the concept of segregation [14] can be examined. Common simulation methods include equation-based, agent-based and Monte Carlo simulations. Equation base simulations apply a set of rules that apply to all objects in the simulation. Agent based simulations examine multiple bodies with different governing rules and how they interact. Monte Carlo simulations rely on a sort of randomness to approximate a solution [15].

Equation based simulations are those that use natural principles that describe the physical behavior of a system. Equation based simulations can be used to study the interaction between individual bodies such as mass-spring-damper systems but can also be applied to fields such as fluids, solid bodies and electrical fields. For example, Bernoullis equation can be applied to develop the relationship between a fluids velocity and pressure drop for a given model. In these simulations the analytic equations that govern a system are applied using the finite difference or finite element method. The differential operators used in Equation 2.2 become approximate differences across uniform increments in either x, y or z. In this instance, the temperature gradient would become

$$\frac{dT}{dm} = \frac{T_{m+1} - T_m}{\Delta m} \tag{2.3}$$

in order to determine the rate of temperature change at a location between the two temperatures T_{m+1} and T_m. As the incremental Δm becomes smaller the accuracy of the solution becomes more accurate. Equation based simulations can perform thousands of these calculations in short period of time and generate a highly accurate solution to a problem that would otherwise take an unfeasible amount of time to solve. Equation based simulation is more commonly used in the scientific and engineering fields.

Agent Based Modeling (ABM) simulations are generally used to study how multiple objects, governed by different rules, interact with each other over time. ABM is used in four basic area: flow, markets, organizations and diffusion [16]. Flow simulations include evacuation and traffic. Market simulations focus on the behavior of the stock market. Organizations use ABM to study operational risk and organizational design. Diffusion simulations study innovation and adoption dynamics. Additionally, topics such as bio-warfare and better understanding of the downfall of ancient civilizations can be examined [17]. ABM may be desirable when "The behavior of individuals cannot be clearly defined through aggregate transition rates" [16].

Monte Carlo (MC) simulations use probability distributions to develop approximate solutions to problems. MC simulations are generally used as a supplemental verification and not necessarily as the primary tool for studying a system [18]. First, a domain or population is defined. Samples are drawn from the population that reflect the actual system being modeled. This data is then analyzed based on the actual principles that govern the actual system. Finally, approximate results are generated with the hope that they closely represent the system [19]. The validity of this type of simulation strongly depends on past data. For example, previous weather patterns inform the person performing the simulation on how to sample the domain in order to accurately predict future weather patterns.

2.2.2 Simulation Quality Criteria

Computer simulations have proven to be a remarkably useful tool for studying and predicting data. However, the validity of a simulations results depend largely on the parameters selected

prior initializing the simulation. Poor mesh quality can yield highly inaccurate results and in some cases can prevent a simulation from generating results all together. A strong mesh will generally contain varying sizes of elements. It is important to have a fine mesh in areas that see large gradients in order to accurate describe what is happening [20]. Regions with little physical variation can support a coarser mesh with small affect on the simulation. Additionally, locations on a model where shape factors change rapidly can cause very non-uniform element shapes and can act as concentration points.

A series of simulation model metrics have been defined that help to characterize the quality of the model and the results obtained. Orthogonal element quality, element aspect ratio and element skewness are a few of the metrics used to validate the quality of a models results. Orthogonal element quality is defined relative to adjacent cells. This metric is a dot product of vectors that describe element centroids and face normal vectors. Orthogonal quality defines the uniformity of a generated mesh. The aspect ratio of an element is defined as the ratio of the longest side of an element to the shortest side of an element [21]. The aspect ratio of a generated element is compared with the idealized shape, either a unit square or equilateral triangle. The idealized version of these shapes has a value of one. The further from the idealized aspect ratio, the more inaccurate a solution becomes. The skewness of an element is a measure of angular deviation from an idealized shape [22, 23]. The maximum angular value of the idealized unit square is 90 degrees, and an equilateral triangle is 60 degrees. The further from these values an elements angle takes, the more unreliable a solution becomes.

Orthogonal mesh quality is important for defining the overall character and validity of a mesh. This metric is defined relative to the centroids of adjacent cells and the vector orthogonal to the face of a cell. Three quantities are necessary to define the orthogonal quality of mesh: the area vector of a cells face, A_i, the centroid of a cells face, f_i, and the centroid of the adjacent cell, c_i. A_i is the vector, normal to face i of a cell, scaled relative to its area. f_i is a vector from the centroid of the element to the centroid of face i. c_i is the vector from the centroid of the element to the centroid of the element adjacent to face i. Two dot product calculations are conducted from these

values and the minimum value is taken to be orthogonal quality for the element being evaluated.

$$min\left[\frac{A_i * f_i}{||A_i|| * ||f_i||}, \frac{A_i * c_i}{||A_i|| * ||c_i||}\right] \tag{2.4}$$

The values in Equation 2.4 are angles measured relative to the face normal vector of a cell. The first angle is between the vector from the cell centroid to the face centroid and the face normal vector. For an ideal element, the centroid is in the barycenter and these vectors would generate an angle of 0 degrees. The second angle is between the vector from the centroid of the element to the centroid of the adjacent element and the face normal vector. For two adjacent, ideal elements the centroids are both in the barycenter and generate an angle of 0 degrees. ANSYS defines the orthogonal quality as: 0-0.001 as unacceptable, 0.001-0.14 as bad, 0.14-0.20 as acceptable, 0.20-0.69 as good, 0.70-0.79 as very good and 0.98-1.00 as excellent [24].

The aspect ratio of an element can be defined two ways. The first is the ratio of the largest length of an element to the smallest length of an element for regular element shapes [21]. The second is the ratio of the radius of a circle circumscribed around an element and the radius of a circle inscribed inside an element for irregularly shaped elements [25]. Aspect ratio is an important metric due to the processing requirements of numerical simulation algorithms. These algorithms perform the same operations on multiple parts of the data simultaneously. This necessitates equal sizing of elements to in order to more accurately calculate the information at each step. The decomposition of a model is used to construct preconditioners which represent the initial problem assumptions [26]. The shape of the elements heavily influences the quality of the preconditioners and it is for this reason that the aspect ratio is such an import metric for generating a quality solution. Additionally, the quality of a models preconditioners effect the solution time of a simulation [25].

In ANSYS, the aspect ratio for an idealized element is one. The further from unity that an element is, the more inaccurate a solution becomes. This is, however, not always true. In areas of a simulation where physical gradients are low, large aspect ratios can still produce adequate results

[20]. Engineering judgment should be employed to balance aspect ratio considerations and time to solution.

Skewness is defined relative to the 2D aspect of a mesh element, the face (Equation 2.5). Elements with high skewness, very large or very small angles, result in distorted element generation. As 3D elements diverge from ideal, the equations generated by ANSYS become skewed, and the more inaccurate a solution becomes. Skewness is calculated based on both the maximum angular value, θ_{max}, minimum angular value, θ_{min}, and the idealized angular value, θ_e. Skewness values range from zero to one. Zero skewness represents and ideal element and skewness increases as angular deviation increases.

$$max\left[\frac{\theta_{max}-\theta_e}{180-\theta_e}, \frac{\theta_e-\theta_{min}}{\theta_e}\right] \tag{2.5}$$

Angular deviation is an important metric for judging a meshes quality because of the way FEM generates solvable equations. The finite element method decomposes the resultant quantities (force, stress, temperature, etc.) at each node of an element into its component quantities. These quantities are organized in a matrix and the governing equations are applied. Large element skewness results in unequal element edges which cause directional bias [21]. ANSYS skewness values are defined as: 0-0.25 are considered excellent, 0.25-0.50 are very good, 0.5-0.80 are good, 0.80-0.94 are acceptable, 0.94-0.97 are bad and 0.98-1.00 are unacceptable [24].

2.3 Thermal Haptics

Thermal sensation is one of the most pronounced and important sensory feedback systems in the human body. The sensory system uses specialized receptors known as thermoreceptors to identify the presence of a thermal stimulus [3]. Thermoreceptors are located through out the skin at various depths and in various concentrations. When a thermal stimulus is present on the skin, thermoreceptors begin to fire signals to the brain. When the brain receives these signals, it interprets them as either hot or cold and responds accordingly. The interpretations of thermal stimuli by the brain affect other areas of human perception as well. For example, skin temperature

has an affect on vibrotactile perception. Colder skin temperatures reduce the bodies ability to perceive vibration applied to the skin while heating is less sensitive to this affect [27]. Additionally, thermal response can be use to help identify certain material properties even with visual stimulation is limited [28, 29].

Thermoreceptors are divided into warm and cold receptors [30] with cold receptors being more prevalent in the human skin than warm receptors at a ratio of thirty-to-one [31]. Additionally, warm and cold receptors respond to different rates of temperature change [5] and are activated at different ranges of temperatures. Warm thermoreceptors are active in the range from 30°C to 45°C. Cold thermoreceptors are active in the range of decreasing temperatures from 30°C to 18°C. Below 18°C and above 45°C, thermal sensation transitions to a feeling of pain which is transmitted through receptor called nocioceptors [32]. However, a sensation of pain can be elicited within these bounds by applying a "thermal grill". Thunberg first discovered this phenomenon in 1896 [33]. When skin comes into contact with alternating rows of hot and cold thermal stimuli, a feeling of pain is generated. The sensation of pain has been shown to be directly related to the magnitude of the temperature difference even when hot and cool temperatures are well below the pain threshold [34].

Thermoreceptor response, as with all types of neurotransmitters, is a function of spatial and temporal summation effects. Spatial summation is the combined effect of multiple stimuli over a specified area of skin. Temporal summation is the total effect of repeated stimuli. In thermal perception, spatial summation shows an inverse relationship with the threshold temperature. As the area of thermal stimulation increase, the perceptible threshold decreases [5]. This affect is more pronounced for heating stimuli than for cooling stimuli. Temporal summation shows a direct relationship with perception. Thermoreceptors send electrical signals to the brain through structures in the body called synapses. These structures act as capacitors [35]. The area and resistance of a cells surface dictates the membranes time constant which determines the rate at which a receptor responds to an external stimulus. If the time constant is sufficiently long, which is the case for a cellular membrane, than the summation is increased [36]. Therefore as the

number of signals passing through a synapse increase, the amplitude of the stimulation increases. Additionally, studied have shown that temporal summation of heat stimuli has an enhanced and prolonged effect on nocioception [37, 38].

The ability to perceive hot or cold sensations is responsible for human safety and comfort. Entire industries are devoted to regulating thermal comfort in homes and commercial building while being as cost effective as possible. The human body is capable of reacting to thermal cues in more ways than just comfort. The ability to elicit a perceived thermal sensation has been demonstrated through the application of a "thermal grill". Additional thermal displays have been studied that help to discern between materials. However, there is still much room for exploration in the field of thermal displays, thermal feedback and thermal perception.

It has been demonstrated that through the application of asymmetrically heated and cooled thermal stimuli, an artificial sense of constant cooling could be achieved [8]. The basic principle behind this is the thermal threshold. This principle states that as the rate of temperature change decreases, larger temperature differences can be applied to the skin without thermal perception. The physical experiment used thermal actuators (peltier devices) to control the rate of temperature change such that if a set of thermal actuators were heating at a rate below the perceptual threshold that the heating would not be noticed. Simultaneously, if a set of actuators were cooling at a rate above the perceptual threshold this sensation would be noticed. In addition, the location of the cooling actuators are constantly changing. The locations of heating and cooling actuators were deliberately chosen as well. In several experiments, the patterns were ordered while in others, the patterns were systematically disordered. Alternating heating and cooling locations was done to ensure that the average skin temperature would not change over time. Physical experiments and computer simulations were performed, with the forearm approximated as a copper cylinder and the skin approximated as a layer of polyurethane rubber, to validate this requirement of the system. This also ensures no location on the skin will be allowed to come into equilibrium with the cooling actuators. With only the cooling sensation being perceptible and by always forcing a thermal gradient, the feeling of constant cooling is achieved.

The physical setup forced some requirements on the heating and cooling ratios. The devices consists of four rows of three actuators. The actuator patterns examined in this study always heat and cool in groups of three. In order to maintain constant skin temperature, one actuator group is at a peak value, 32.5°C, one group is at a minimum value, 31.5°C and two actuator groups are heating/cooling. The temperature profile is therefore required to hold a three/one heating cooling ratio. All timing patterns are scaled according to this with 21/7, 30/10 and 45/15 heating/cooling being the primary rates.

In the experiment performed by Manasrah et al. [8], the perception of constant cooling is delivered by an induced temperature gradient on the skin. The rate of heating and cooling, °C/s, was varied for different experiments to see what rates would produce the strongest sense of cooling. This temperature rate is what drives the thermal gradient in the skin. This means there is a constantly changing thermal gradient present in the skin and therefore an associated heat flux acting on the skin. The temperature difference and therefore heat flux is what is examined in this study and it is this quantity that we wish to better understand. This leads to the following open questions:

- Is the magnitude of heat flux what drives perception?
- Is the rate of change of temperature that leads to stronger perception?
- Is the direction of heat flux a primary factor?
- Is the ratio of perimeter to area upon which the heat flux is located the prime factor?
- Does perception trigger at a certain value of heat flux?
- If triggered, does perception persist or does it gradually fade if a certain heat flux value is not maintained?

The aim of the proceeding chapter is to answer these questions as well as gather information that will allow for the prediction of thermal perception. Additionally, the ability to maximize and sustain the perception of the thermal display is examined.

Chapter 3: Heat Flux Associated with Heating and Cooling Cycles

This chapter examines the heat flux associated with the asymmetrically heated and cooled thermal display developed by Manasrah et al. [8]. Three sets of simulations are performed throughout this chapter. First, a preliminary examination of the isolated heating and cooling segments is performed. Analytic calculations are performed based on the boundary conditions of the physical setup which will serve as a validation of the subsequent simulations. These individual heating and cooling segments are combined to create the actual patterns examined. The experimental patterns used to achieve constant cooling are simulated in order to gain an insight on heat flux profiles seen in the skin. Based on the heat flow characteristics of the isolated segments and the combined patterns, a theoretical first approximation of the relationship between heat flux and thermal sensation is developed. The last set of simulations is a new set of patterns with altered timings and spatial variations. This is done with the intention of finding more efficient patterns to try in future experiments. It should be noted that throughout this chapter, use of directional notation, Cartesian and cylindrical, is interchangeable. The angular dimension is identical to the x-direction, the radial dimension is identical to the y-direction, and the axial dimension is identical to the z-direction. The focus in this thesis is the centerline of the cylinder assembly. At this location, the cylindrical and Cartesian coordinate systems coincide and therefore are used interchangeably.

3.1 Heat Flux: A Theoretical Analysis

The work done by Manasrah et al. [8] demonstrated that a perception of constant cooling was possible. Additional work was done to validate the temperatures apparent in the system. This was done by creating a model of the actual experiment. The model consisted of a copper and polyurethane hollow cylinder to approximate the internal parts of the body and skin, respectively.

Thermal actuators (Peltier devices) used in the actual experiments were included in the model in order to manipulate temperature. Simulations were conducted to verify the temperatures in conjunction with the physical model.

Equation 2.1 is used to determine the heat flux values produced at different times during the heating and cooling segments of the thermal actuators. Equation 2.1 can be used in a number of different ways to gain insight on the heat flux values produced by the system. This equation can be applied in an exact fashion given the temperature profile of a system. The differential of the temperature distribution can be taken and then a specific location and time can be specified to calculate the heat flux. This is the most exact method, however, the temperature profile is often large, complex and time consuming to calculate, making it undesirable method. An alternative method is to make the differential an approximate delta value where the difference in temperature at both ends of an object is taken and then divided by the distance between them. This is an approximation of the heat flux in a system, but if applied to specific circumstances, may be a reliable estimate.

3.1.1 Analytic Solution to the Heat Equation

The analysis of the heat flux values present in the system will be limited to the radial direction of the hollow cylindrical coordinate system. Heat flux in the radial direction in hollow cylindrical coordinates is expressed the same as in Equation 2.1. The heat flux at the interface of the actuators and the polyurethane cylinder are evaluated for four cases representing individual heating and cooling segments. Additionally, because the surface flux is being examined, the differential will become a delta approximation and Equation 2.1 becomes:

$$q_r'' = -k * \frac{\Delta T}{\Delta r} \tag{3.1}$$

Positive heat flux is defined in the direction of decreasing temperature gradient which necessitates the negative sign in front of the equation. In this system, heat enters the medium from

the outer radius of the hollow cylinder and therefore the heat propagates in a negative coordinate direction. This means that to define positive heat flow (heat entering a system), the negative sign is negated.

3.1.2 Isolated Heating and Cooling Segments

Four distinct cases will be examined using Fourier's Law in the radial dimension. Later, the same four heating/cooling cases will be examined through ANSYS transient thermal simulation. The examination will be limited to the 30/10 heating/cooling rate. These four cases are evaluated in order to have an understanding of the expected heat flux values produced in the system. Additionally, these four cases are reproduced using simulations in order to verify their accuracy. The four cases to be examined:

- Case 1: Actuator heating 1 degree over 30 seconds with its initial temperature equal to skin temperature, 32°C, and increases one degree to 33°C
- Case 2: Actuator heating 1 degree over 30 seconds with its initial temperature half a degree lower than skin temperature, 31.5°C, and increase one degree to 32.5°C
- Case 3: Actuator cooling 1 degree over 10 seconds with its initial temperature half a degree higher than skin temperature, 32.5°C, and decreases one degree to 31.5°C
- Case 4: Actuator cooling 1 degree over 10 seconds with its initial temperature equal to skin temperature, 32°C, and decreases one degree to 31°C

The internal temperature of the body is taken to be 32°C and therefore this is the temperature given to the copper cylinder. The temperature differential is taken as $T_{int} - T_n$ where T_{int} is internal temperature at 32°C and $T_n = T(t_n)$ is the temperature at t_n. It is hypothesized that, because of the identical temperature differential of all four cases, similar heat flux values and patterns will be present. Additionally, a linear heat flux plot proportional to the temperature profiles in Figure 3.1 is expected.

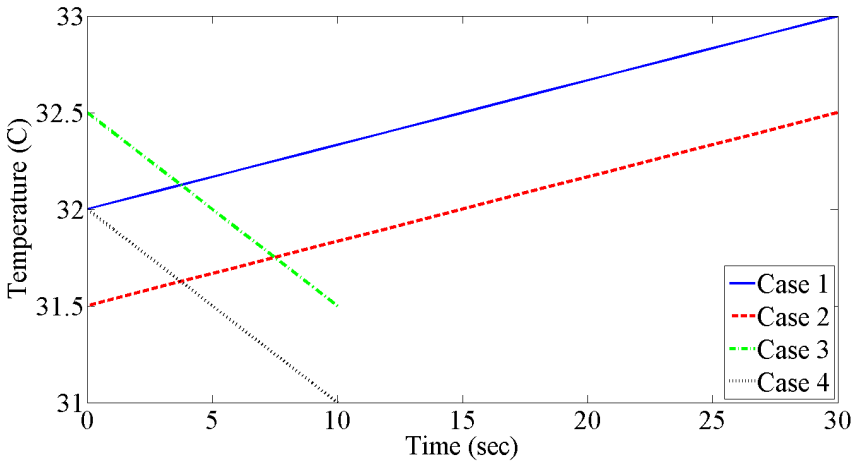

Figure 3.1: Four isolated heating and cooling segments. The four cases representing the 30/10 heating/cooling rate are seen graphically.

3.1.2.1 Heating From Skin Temperature

It is expected that the initial heat flux will be 0 W/m^2 when heating from skin temperature as the initial temperature differential is 0 °C; internal body and initial actuator temperature are both taken as 32°C. As the temperature increases, the heat flux will increase linearly and proportionally. Figure 3.2 shows this behavior. The initial heat flux value is 0 W/m^2 increasing linearly to 150 W/m^2.

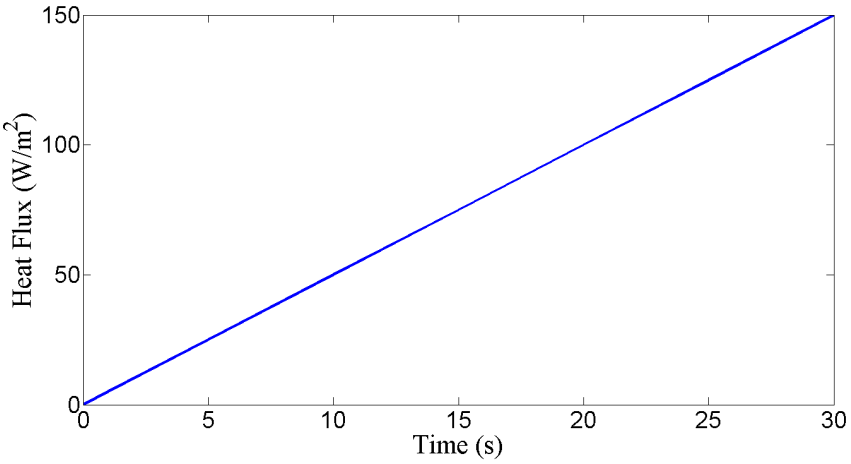

Figure 3.2: Analytic case 1 using Fouriers equation to calculate the heat flux profile for the scenario where the temperature increases one degree from skin temperature over 30 seconds.

3.1.2.2 Heating From Below Skin Temperature

It is expected that a negative initial value for heat flux with a positive slope will be present when heating from below skin temperature,. This is due to the negative temperature differential; internal body temperature at 32°C and initial temperature at 31.5°C. An initial heat flux of -75 W/m^2 is calculated. Due to the symmetry of the heating pattern, at $t/2$ when the temperature differential becomes 0 °C, a heat flux of 0 W/m^2 is observed. The positive slope is present throughout the heating process and the final heat flux value is equal in magnitude and opposite in direction as the initial value at 75 W/m^2.

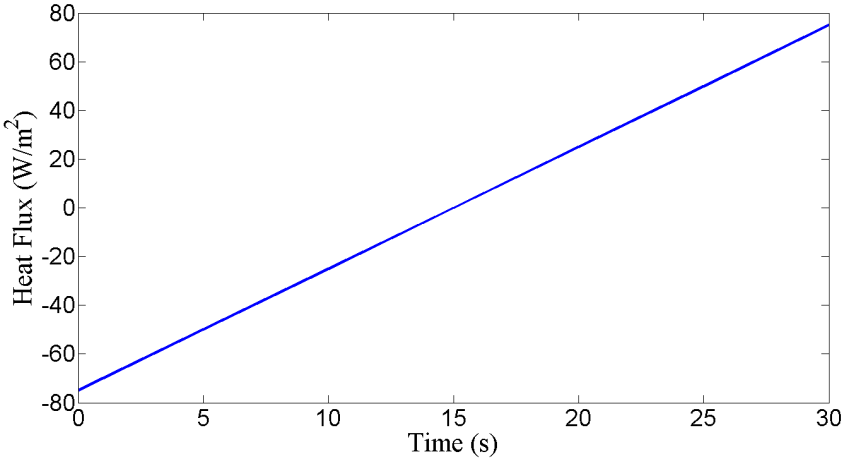

Figure 3.3: Analytic case 2 using Fouriers equation to calculate the heat flux profile for the scenario where the temperature increases one degree from below skin temperature over 30 seconds.

3.1.2.3 Cooling From Above Skin Temperature

Case 3 is the first cooling segment with cooling beginning half a degree above skin temperature. As the initial temperature is above skin temperature, a positive initial heat flux with a negative slope is expected. This is indeed the initial behavior observed. The positive initial temperature differential creates a heat flux of 75 W/m^2 with a decreasing trend. The symmetry seen in the case 2 is present in case 3 and at $t/2$, with the temperature differential at 0 °C, the

heat flux reaches a value of 0 W/m^2. Heat flux continues in the negative direction and ultimately reaches a symmetric final value of -75 W/m^2.

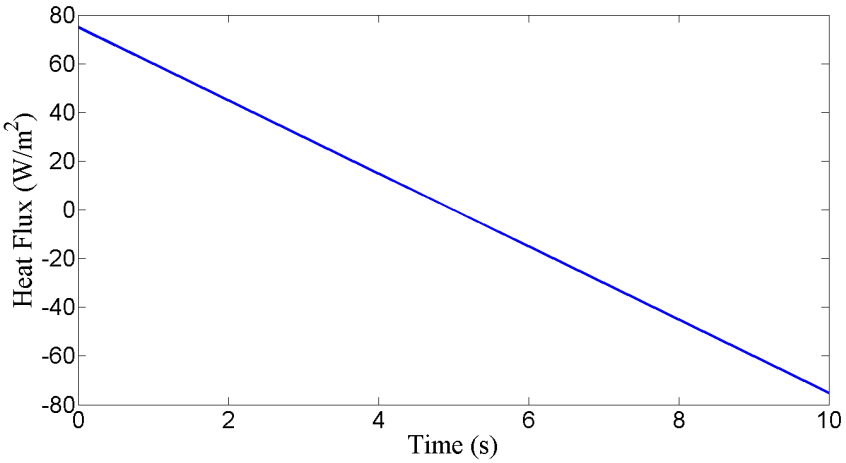

Figure 3.4: Analytic case 3 using Fouriers equation to calculate the heat flux profile for the scenario where the temperature decreases one degree from above skin temperature over ten seconds.

3.1.2.4 Cooling From Skin Temperature

Case 4 shows the heat flux values for the case where cooling begins at skin temperature. The initial temperature differential is 0 °C and therefore produces a heat flux of 0 W/m^2. The heat flux takes a negative slope, proportional to the decreasing temperature differential. The final heat flux value is -150 W/m^2. This is similar in magnitude and opposite in direction to the behavior of case 1. This is expected due the similar temperature gradient which is a spatial differential and not a temporal differential.

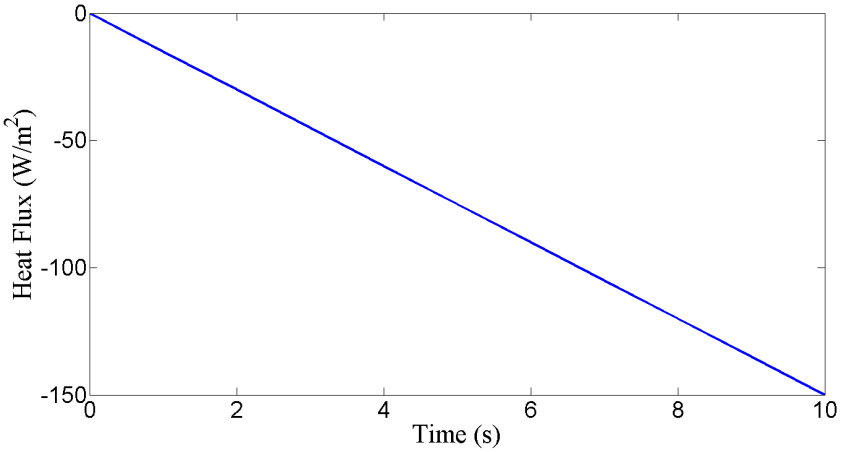

Figure 3.5: Analytic case 4 using Fouriers equation to calculate the heat flux profile for the scenario where the temperature decreases one degree from skin temperature over ten seconds.

3.2 Simulated Haptic Model

The method for analysis in the study was to create a 3D model representing the physical setup used in the original experiment. Two unique pieces of software were used in conjunction with each other: Solidworks for creating the physical model and ANSYS Workbench for analyzing the experiment using Finite Element Analysis (FEA).

Solidworks was used to create a series of models for analysis. The standard model used in the actual experiment was the first and primary model used throughout this study. The standard model consisted of three components used in the experimental setup: a copper cylinder, a polyurethane rubber cylinder and aluminum actuators known as peltier devices. The copper cylinder was used to simulate constant internal body temperature. The copper cylinder was in direct contact with the polyurethane cylinder. The polyurethane rubber was used as a medium to represent human skin. Polyurethane rubber was chosen because it has similar thermal properties as that of skin (Table 3.1). The aluminum peltier devices were used to generate the oscillating temperature rates and patterns. Additionally, several models were created to observe the effects of changing the axial spacing between actuators. This was done to determine at what spacing the heat

flux in the z direction becomes dominant over the heat flux in the y direction for the space between actuators.

Table 3.1: Thermal properties of human skin and polyurethane rubber.

Material	Density (kg/m^3)	Heat Capacity (J/kg*K)	k (W/m*K)
Skin	1062	3400	0.29
Polyurethane Rubber	1200	1800	0.3

ANSYS Workbench was employed to run many types of thermal transient heat transfer simulations. Simulations were run on the individual heating and cooling segments of the actuators. This was done to better understand the heat flux values seen and how the timing rates affected the global minimum and maximum values of heat flux as well as to gain a baseline understanding of the heat flow in the model. Additionally, these simulations were done in order to check accuracy between the analytical and simulation analysis. Following these baseline simulations, actual spatial and temporal patterns used in the physical experiment were analyzed. This was done to develop a correlation between temperature perception and heat flux. The final set of simulations were a series of new and rearranged spatial patterns as well as several new timing patterns. This was done in an attempt develop a new, optimized physical experiment.

3.2.1 Solidworks Model

In order to create the appropriate 3D model for simulation analysis, the Computer Aided Design (CAD) software Solidworks© was used. The different components of the cylinder assembly were modeled separately and combined in order to develop the most accurate model possible. The copper cylinder has an inner and outer radius of 37.05mm and 38mm respectively. The polyurethane cylinder has a thickness of 2mm leading to an inner and outer radius of 38mm and 40mm respectively. Two millimeters thickness was chosen because that is the approximate thickness of human forearm skin. Both the copper cylinder and the polyurethane cylinder are 304.8mm. The aluminum actuators have a cross-sectional area of 225mm^2 or 15mm x 15mm

with a thickness of 3.8mm. Measurements for the cylinder are summarized in Table 3.2 and are illustrated in Figure 3.6.

Table 3.2: Dimensions used for model creation.

Component	Dimension	Value
Actuator	Length	15mm
Actuator	Width	15mm
Actuator	Height	3.8mm
Actuator Spacing	Axial	5mm
Actuator Spacing	Angular	27°/4mm
Copper Cylinder	Inner Radius	37.05mm
Copper Cylinder	Outer Radius	38mm
Copper Cylinder	Length	304.8mm
Polyurethane Cylinder	Inner Radius	38mm
Polyurethane Cylinder	Outer Radius	40mm
Polyurethane Cylinder	Length	304.8mm

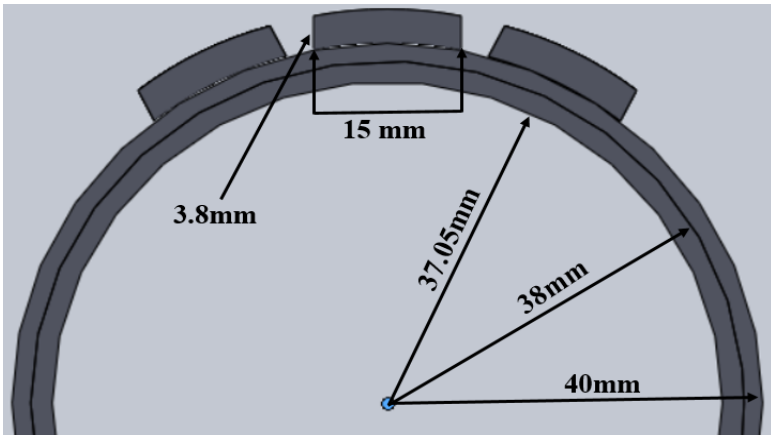

Figure 3.6: Cross-sectional view showing the dimensions for the cylinder.

The general process for creating the cylinder model is to make a 2D sketch with the proper dimensions in Figure 3.6 and then using the extrude tool in Solidworks to generate the 3D model. For the copper and polyurethane cylinder the process involves drawing two circles (of appropriate diameter) then placing a “concentric” constraint on the two circles. The “concentric” constraint ensures that the thickness of both cylinders in uniform about their central axes.

Modeling the thermal actuator meant creating the internal face which is in contact with the outer surface of the polyurethane cylinder. In order to ensure the proper area of contact between actuator and polyurethane, the chord length was calculated based on a 15mm arc length. The chord segment was sketched and then the arc length segment was created using the end points of the chord segment and was given the proper radius dimension (Figure 3.7). Vertical lines were sketched to give the proper thickness to the actuator, 3.8mm, and finally the top section of the actuator was drawn. This object was extruded to 15mm to give the exact area of 225mm^2.

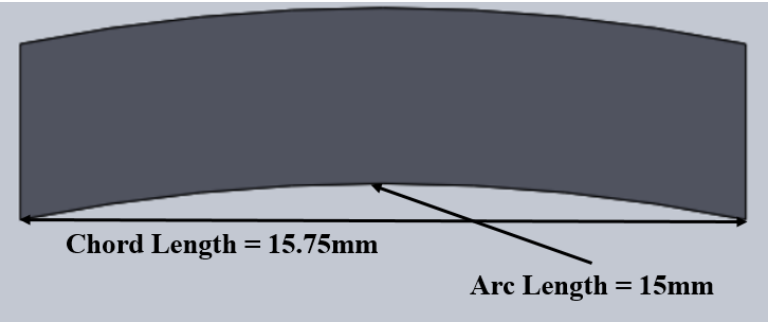

Figure 3.7: Chord length and arc length used to create the actuator cross section.

All of the individual components are then brought into the assembly environment. The copper cylinder is placed at the origin and given the "Fixed" constraint. This constraint fixes the cylinder in space and ensures the subsequent components are placed properly with respect to each other. The polyurethane cylinder is added to the assembly and given a "concentric" constraint relative to the copper cylinder. The flat faces of each cylinder are then made parallel to each other to ensure proper alignment. One single actuator is brought into the assembly and the internal face of the actuator and the exterior face of the polyurethane cylinder are mated using the "concentric" constraint. The mid plane of each object (actuator and polyurethane cylinder) is made parallel for proper alignment. Finally, the flat faces of the actuator and polyurethane cylinder are given an offset distance. The offset distance was chosen to be 120mm. To ensure proper spacing between actuators the "pattern" feature was used to create the remaining actuators. The "linear pattern" was used to create a parallel row of four actuator with a five millimeter spacing between actuators.

The “circular pattern” feature was then used to create two additional rows of parallel actuators on either side of the centerline of actuators (Figure 3.8).

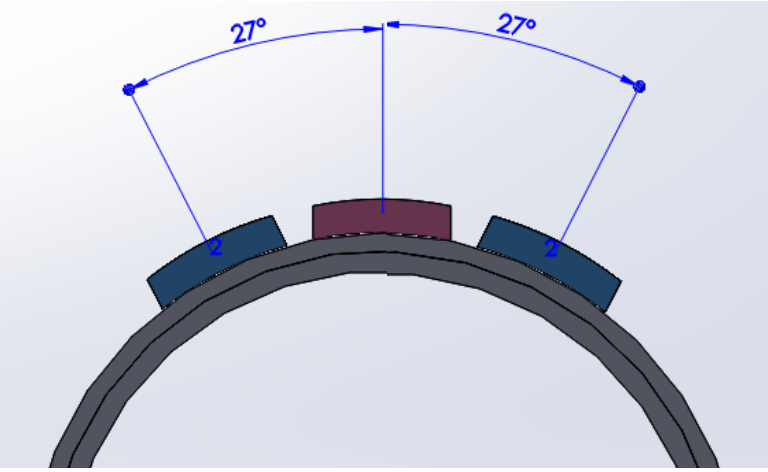

Figure 3.8: Angle offset of actuators relative to the centerline of actuators.

A series of additional models were created with varying axial spacing. All modeling parameters were held constant with the exception of the distance chosen when creating the linear pattern. The standard model consisted of five millimeter spacing. Three additional models were made using zero millimeter spacing (touching actuators), ten millimeter spacing and 15 millimeter spacing. The final step in creating the cylinder assembly model is to save it as a STEP file. The STEP file format allows the simulation software to easily import, manipulate and analyze the assembly.

3.2.2 ANSYS Transient Thermal Setup

ANSYS Workbench has the ability to run many types of physical simulations that are used to compare real world experiments. The Transient Thermal analysis is used to simulate systems with non-constant temperature boundary conditions. ANSYS Transient Thermal analysis uses FEA to calculate temperatures, based on boundary conditions and material properties, at discrete nodes generated by a meshing process that is performed by the software. In any simulation, there is the possibility that the results may not accurately represent the physical phenomena. If the mesh

that is generated does not meet specific criteria, the results can be off by orders of magnitude and may not converge on a solution at all. If the time stepping is not within a certain range the results may be skewed. If the proper geometric considerations are not detailed, ANSYS may not be able to begin the simulation. There are several steps and precautions required to ensure accuracy of the results.

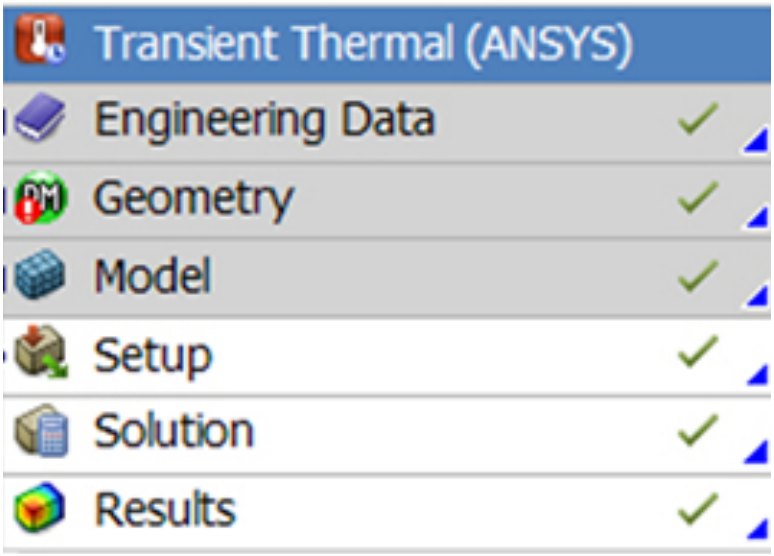

Figure 3.9: ANSYS transient thermal setup screen. This is where all the simulation setup information is specified.

The higher level Transient Thermal setup consists of six steps: Engineering data, Geometry, Model, Setup, Solution and Results. Engineering data consists of material selection. ANSYS has the physical properties of many materials built into the system. However, the user is also given the ability to add a specific material not already in its library. This functionality was actually used for this study to specify the exact polyurethane rubber employed in the experimental studies. Geometry is where the 3D model is specified. The user has the ability to create 3D models in ANSYS Design Modeler. Files from external modeling software can be imported but have to be in a specific format. For this study, the STEP file format was used to import a 3D model created in Solidworks. The Model section is where the actual simulation parameters are specified. This includes coordinate systems, meshing and analysis settings. Setup and Solutions are also specified

in the Model environment and generated by the software. Finally, Results are the actual generated data from the simulation. The Results sections is where the temperature and heat flux information is contained. The format for setup is seen in Figure 3.9. The materials and geometry are specified at this point of the simulation setup process.

In the Engineering Data section, structural steel is the default material selected by ANSYS. Aluminum and Copper must be chosen manually. Polyurethane rubber must be specified and its thermal properties input into the system (Figure 3.10). Other properties may also be set in this section. Fluid properties, convective properties and non-linear materials may also be specified. These options were not used in this study.

Outline of Schematic A2: Engineering Data

	A	B	C	D
1	Contents of Engineering Data		Source	Description
2	Material			
3	Aluminum Alloy			General aluminum alloy. Fatigue properties come from MIL-HDBK-5H, page 3-277.
4	Copper Alloy			
5	Structural Steel			Fatigue Data at zero mean stress comes from 1998 ASME BPV Code, Section 8, Div 2, Table 5-110.1
6	Polyurethane			
*	Click here to add a new material			

Properties of Outline Row 6: Polyurethane

	A	B	C	D	E
1	Property	Value	Unit		
2	Density	1200	kg m^-3		
3	Isotropic Thermal Conductivity	0.3	W m^-1 C^-1		
4	Specific Heat	1800	J kg^-1 C^-1		

Figure 3.10: ANSYS material selection. Aluminum and Copper are selected manually where as Polyurethane Rubber is input into the system with the proper material specifications.

Inside the geometry setup, the ANSYS Design Modeler is used to import and prepare the 3D model for simulation. In Design Modeler, there are several tools required for proper meshing of the model: Import external geometry, Generate, Form new Part and the Share Topology: Imprints tool. The "import external geometry" function is the first tool used. This brings the CAD file (in

the STEP format) into the modeling environment. The "generate" function is required in order for the file to become an object inside Design Modeler which can then be further manipulated. The "Form new Part" tool is then used to allow ANSYS to see the model as one part consisting of multiple bodies instead of fourteen individual bodies. This allows for more conformal meshing in ANSYS. The last tool used to create a high quality mesh is the "Share Topology: Imprints" function. When multiple bodies come into contact with each other, the mesh generated between the bodies can be inconsistent because the nodes on each body may not coincide with each other. The heat flux between the actuators and polyurethane cylinder is the primary focus and therefore a very well defined contact region is desired. The "Imprints" tool accomplishes this.

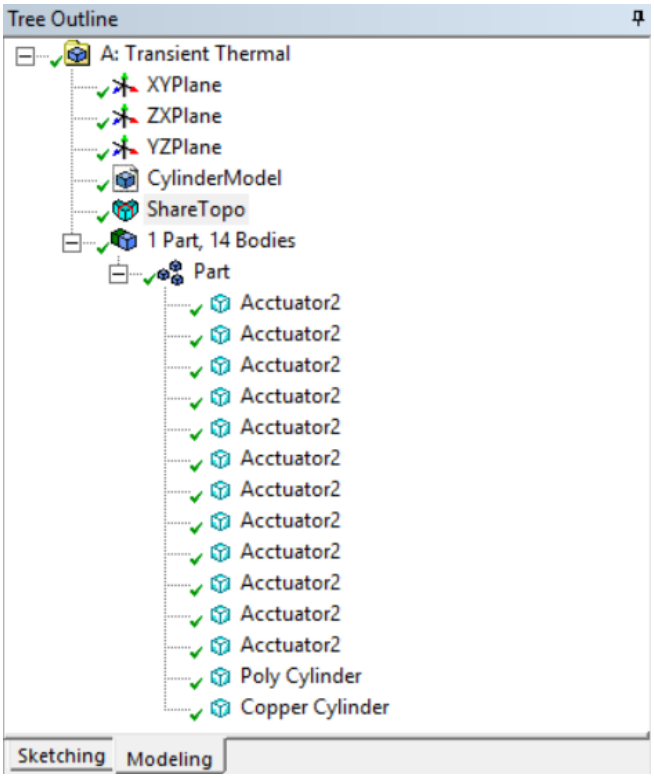

Figure 3.11: Geometry setup in ANSYS design modeler. The 3D model is imported into ANSYS. A new part is formed consisting of all individual bodies. Share topology: Imprints is used to create a continuous mesh across bodies.

Note that the part generated by the "Form new Part" tool is the where the "Share Topology" tool is applied. This ensures that interfaces between bodies will have a continuous mesh. Figure

3.11 shows all of the manipulation done to the CAD model in order to generate a proper mesh. The mesh quality is very important for accurate solutions. A series of mesh quality metrics are generated and will be discussed in a later section.

3.2.2.1 Simulation Parameters

Inside the "Model" section of the Transient Thermal setup is where the parameters that control the simulation are selected. The parameters in this section are broken into three parts: Model, Transient Thermal and Solutions. Model consists of: Geometry, Coordinate System, Connections, Mesh. Transient Thermal is comprised of: Initial Temperature and Analysis Settings. This section is where the boundary conditions are specified as well. Solutions is where the output values such as temperature and heat flux are specified. The simulation outline is seen in Figure 3.12.

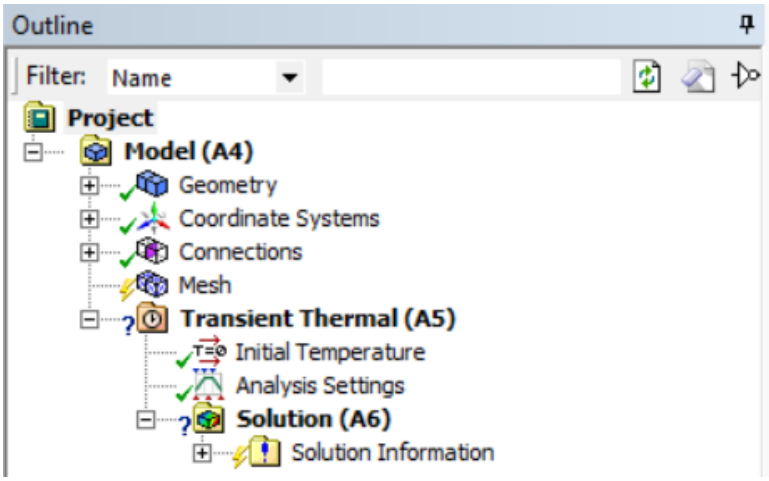

Figure 3.12: ANSYS simulation tree outline. All of the parameters that control the simulation are specified at this point in the simulation setup process.

"Geometry" is where the material properties are applied to each object in the 3D model. Aluminum is applied to the twelve aluminum actuators. The polyurethane rubber cylinder and the copper cylinder are assigned their respective materials. "Coordinate System" is where specific locations can be selected for analysis. This option allows the user to define an x, y and z coordinate

location as well as the orientation of the coordinate system. These locations are later used to place objects known as "Probes" throughout the solid model that collect specific information at areas of interest. For example, this is used in order to place the temperature and heat flux probes at locations under and between actuators. "Connections" is where the contact locations between difference bodies is specified. However, because the "Share Topology: Imprints" was specified earlier these contact locations have already been specified. "Mesh" is where the actual mesh parameters are specified. There are many types of mesh specifications but because of the way this model has been controlled to this point, only one type of mesh control is required for adequate meshing. In this case, only the "Contact Sizing" mesh tool is necessary. "Contact Sizing" states the size of the mesh at the interface of two bodies.

Under the "Transient Thermal" section, the initial temperature is specified. This is the temperature seen in the model at time equals zero,

$$T(x,0) = T_i \tag{3.2}$$

in this case, 32°C. The analysis settings are where the length of the simulation is stated. Time stepping is also specified at this point in the simulation setup. Boundary conditions are created in this part of the setup. This is where the constant internal temperature of 32°C is placed. Additionally, the spatial patterns and timing patterns are a stated here. A total of five temperature conditions are created here: one internal temperature and four actuator temperature patterns.

The final requirement for a successful simulation is specifying the output quantities. The "probes", discussed previously, are used in ANSYS to gather the desired physical quantities generated throughout the course of a simulation. The locations of these probes are based on the individual coordinate systems created earlier in the setup. Once all the simulation parameters have been specified, the simulation is ready to be started.

3.2.2.2 Nodal Convergence Study

When running simulations, an important aspect is the ability to properly mesh a model. The mesh characteristics have a major impact on the quality and accuracy of the results. This meshing process generates a discrete set of nodes to be created and then analyzed using numerical methods. Meshs can be large or small, depending on the geometry but generally the smaller the size of the mesh chosen, the more accurate the results of the simulation. However, as the mesh size decreases, the time to solve increases greatly. In addition, as more solution outputs are requested, that time to solution is increased even more. Therefore it is desirable to determine at what mesh size the solution output becomes stable in order to balance accuracy with time to solution.

In order to determine a mesh size that will produce accurate results while solving in a reasonable time, a nodal convergence study is performed. A nodal convergence study is the process of running the same simulation several times, under identical conditions and solution settings, with the only varying parameter being the mesh size. For this convergence study, the initial mesh size selected was 5 mm. The mesh size of each subsequent simulation decreased at regular intervals. Below 2 mm, the mesh size increments varied slightly and became smaller in order to gain more detailed insight into how the mesh quality was changing.

The simulation for this study consisted of a constant initial temperature and constant internal temperature at 32°C. All actuators were at a constant temperature of 32.5°C at the start of the simulation. Two probes were placed in the simulated skin at a depth of 1mm. Probe 1 was located directly under the center of the first actuator and Probe 2 was placed 2.5mm from the edge of the first actuator which is the midpoint between the first two actuators.

The quantities collected for this convergence study included: mesh size, number of nodes, number of elements, the heat flux in x, y, z and total magnitude, mesh quality, aspect ratio and skewness. The quality metrics are collected because they are important to for determining the caliber of the mesh and therefore the accuracy of the solution. Ideal characteristics include high mesh quality, low aspect ratio and low skewness. Table 3.3 indicated that acceptable mesh quality

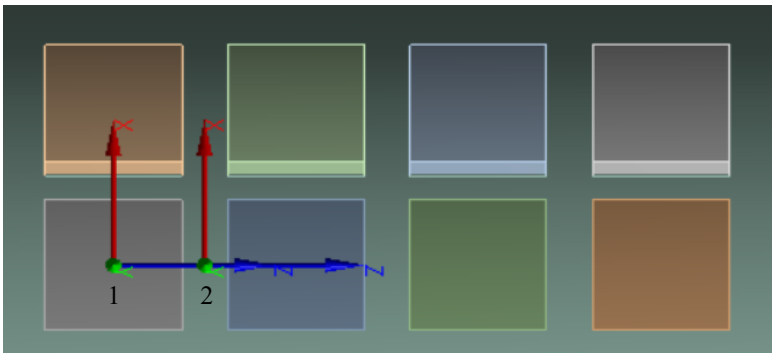

Figure 3.13: Probe locations for nodal convergence study. The values obtained at these locations define the quality of solution obtained from the simulation.

appears around 2.5 mm mesh size, however, to obtain an even higher quality solution, a smaller mesh is chosen.

Table 3.3: Nodal convergence metrics.

Mesh Size (mm)	Nodes	Elements	Total Flux Under (W/m^2)	Total Flux Between (W/m^2)	Mesh Quality	Aspect Ratio	Skewness
5	31843	8949	72.9	22.6	0.405	4.472	0.641
4	29573	7763	63.8	37.2	0.422	5.096	0.613
3	43204	13232	75.3	49.2	0.512	3.662	0.554
2.5	48395	14890	74.9	10.7	0.559	3.395	0.513
2	46811	13987	75.1	7.9	0.622	3.408	0.432
1.8	50388	15854	75.1	9.7	0.640	3.252	0.423
1.5	86983	32064	75.8	8.8	0.640	2.725	0.429
1	158847	58198	74.9	13.9	0.777	2.169	0.309
0.9	172015	65235	74.6	11.7	0.769	2.179	0.324
0.8	200781	82000	74.8	7.8	0.756	2.215	0.343

We can see from Table 3.3 and Figure 3.14 that convergence begins at a mesh of about 2.5 mm. To ensure a highly accurate simulation, a smaller mesh was chosen at 1 mm. Time to solution was not a measured quantity in this study but it was observed that the difference from a 2.5mm mesh to a 1mm mesh was negligible and the smaller mesh was chosen for use throughout the course of this thesis.. The meshed cylinder geometry can be seen in Figure 3.15.

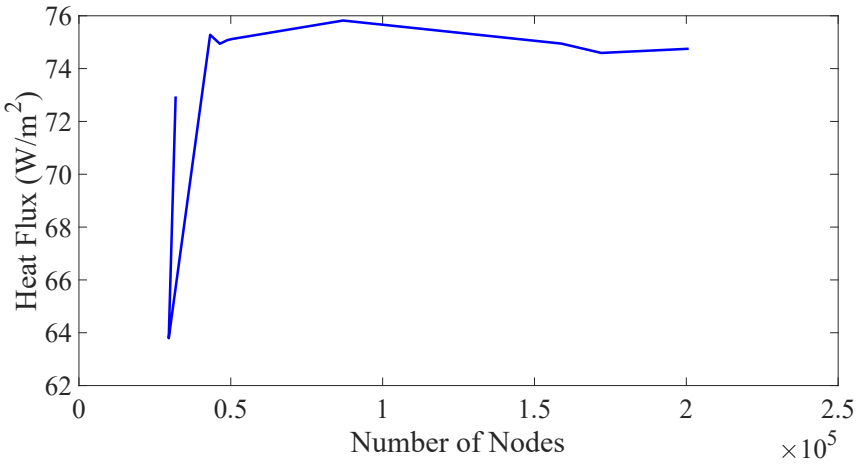

Figure 3.14: A graphical representation of the heat flux values generated for a series of mesh sizes. The heat flux values represent the total heat flux generated directly under the center of one actuator at 1mm in skin depth.

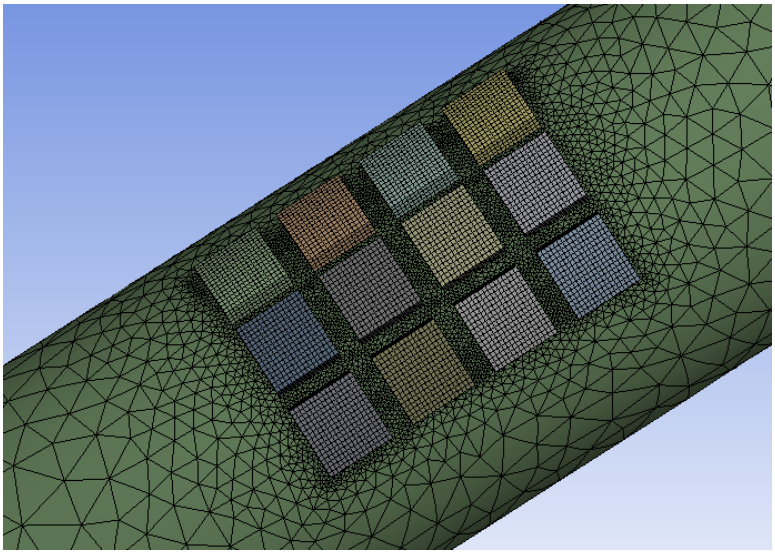

Figure 3.15: 1mm mesh generated on cylinder.

The values listed above have pertained to the average value, over the entire mesh, for each quality metric and at a 1mm mesh, the average values are reasonable enough to assume that the solutions are valid. This scope includes the outer boundaries of the cylinder where little or no heat transfer occurs. However, going one step further and generating the same 1mm mesh on the isolated area of interest, the area immediately around and between the actuators where all the heat

flow occurs, a more accurate description of the mesh quality is observed. For the updated scope of interest for mesh quality, the orthogonal quality becomes 0.789, the aspect ratio becomes 2.004 and the skewness becomes 0.294. All mesh quality statistics have improved and are now well within acceptable values for a proper mesh.

3.2.2.3 Initial and Boundary Conditions

Initial and boundary conditions of a simulation are selected based on how accurately they represent a physical system. In the context of this thesis, the initial condition is selected as 32°C to represent uniform skin temperature. The boundary conditions are selected as a constant internal temperature of 32°C and the external temperature is selected such that it represents the changing actuator temperature (temporally and spatially), in this case oscillating between 31.5°C and 32.5°C.

In ANSYS, a body, face or point can be selected to have a temperature applied to it. For all simulations in this thesis, individual bodies were selected in order to manipulate temperature as opposed to selecting the interfaces between mated components e.g., between copper and polyurethane cylinder, and polyurethane cylinder and aluminum actuators. This was done because it was assumed that, after transient effects were accounted for, the entire body of the Peltier device was at a uniform temperature. This was examined to ensure the same heating patterns were present regardless of whether the body or face was heated or cooled. Two simulations were performed with all actuators heating one degree from skin temperature, 32°C to 33°C. In one simulation, the entire body of the actuator is heated and in the second, only the face of the actuator in contact with the polyurethane cylinder is heated. Heat flux in the y-direction is plotted in Figure 3.16. It is seen that identical results are produced when applying a temperature to the actuator body as with applying the same temperatures at the interface between the actuator body and polyurethane cylinder which verifies the initial assumption. Therefore, for the remainder of this thesis, the actuator body will be selected for temperature actuation.

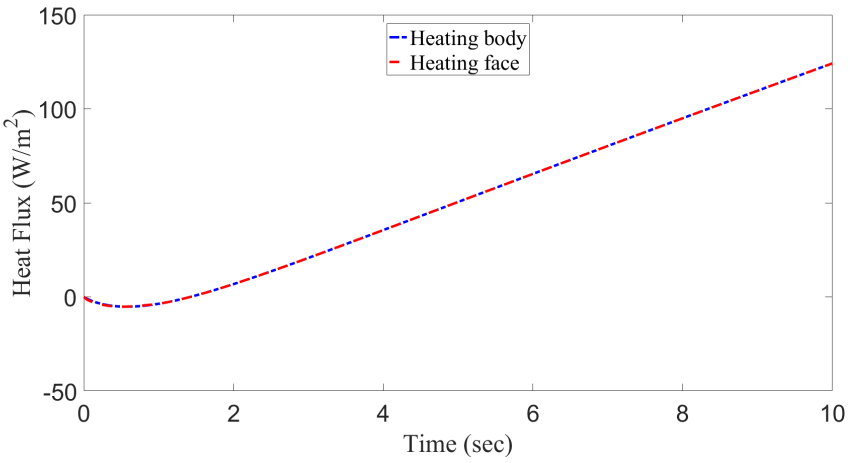

Figure 3.16: Heat flux produced when temperature is applied to body vs. face. The effects of heating the actuator body versus the actuator face in simulation results are shown as a verification for the methods used to evaluate future simulations.

3.3 Heat Flux: A Simulated Analysis

Commercially available simulation software ANSYS uses the finite element method (FEM) for modeling and evaluating systems. FEM is often used to solve complex systems governed by complex partial differential equations that are sometimes impossible to solve analytically. A common example for the use of FEM is computational fluid dynamics (CFD) where the Navier-Stokes equation is utilized even though it cannot be solved analytically. In the following section, the four cases seen in Section 3.1 will be simulated through ANSYS Workbench using finite element analysis. The results will then be compared and reasons for any differences will be evaluated. This, in combination with the analytic analysis above, serve as further proof of the accuracy and validity of the simulations performed later in this thesis.

3.3.1 ANSYS Numerical Method of Solving the Heat Equation

ANSYS uses a consistent method for solving systems using FEM. The methodology consists of three phases: preprocessing, solution and post-processing. The preprocessing phase consists of creating and meshing the model, defining the shape function which describes the interpolation of data between nodes, developing the equations for an element, assembling the elements to

describe the entire system and applying boundary conditions. The solution phase solves the set of algebraic equations developed in the prepossessing phase in order to obtain nodal results, such as temperature. The post-processing phase utilized the nodal results and determines the final values of interest, such as heat flux [39].

The modeling and meshing steps have been described in Section 3.2 and shape functions are chosen internally by ANSYS. Once the model is created and the proper steps are taken to ensure high quality solutions, ANSYS takes the general heat equation and applies the specified boundary and initial conditions to develop the set of algebraic equations that will be applied to the model. The general heat used by ANSYS in matrix form is seen in Equation 3.3 [24, 39].

$$\rho c \frac{\partial T}{\partial t} + [L]^T [q] = \dddot{q} \tag{3.3}$$

where, ρ is material density, c is heat capacity, $\frac{dT}{dt}$ is the temperature gradient in x, y and z, $[L]$ is the differential operator for x, y and z, $[q]$ is the heat flux vector in x, y and z, and $\dddot{q}$ is the volumetric heat generation. Following this, Fourier's law (Equations 2.1) is applied to determine the heat flux as a function of the temperature gradient; this too is done in matrix form:

$$[q] = -[D][L]T \tag{3.4}$$

where, $[D]$ is the thermal conductivity in x, y and z, and T is the Temperature as a function of x, y, z and t.

Combining Equations 3.3 and 3.4 we obtain the matrix form of the heat equation used in ANSYS transient thermal:

$$\dddot{q} + ([L]^T([D][L]T)) = \rho c \frac{\partial T}{\partial t} \tag{3.5}$$

Equation 3.5 is the general form used in all ANSYS thermal transient simulations. ANSYS uses a time integration procedure based on the generalized Euler scheme to perform time stepping operations in transient thermal simulations. The Euler method selects a time step based on the Fourier and Biot number. These two numbers are dimensionless quantities that help to define time

dependent conduction problems [10, 40].

$$Fo = \frac{\alpha \Delta t}{(\Delta x)^2} \qquad \text{and} \qquad Bi = \frac{h \Delta x}{k} \tag{3.6}$$

where, the Fourier number is the ratio of diffusive effects to the storage rate of a body and the Biot number is the ratio of internal conduction effects to external convective effects. If the Biot number is sufficiently small, as is the case for the entirety of this thesis due to the lack of convection, the time step is a function of only the Fourier number. The generalized Euler scheme is seen as:

$$[T^{p+1}] = [T^p] + (1-\theta)\Delta t[\dot{T}^p] + \theta \Delta t[\dot{T}^{p+1}] \tag{3.7}$$

where, $\frac{1}{2} \leq \theta \leq 1$, Δt is the time step as a function of Fourier number, p is the previous time step and, $p+1$ is the current time step.

The default ANSYS setting is with θ = 1 in which case it is called Backward Euler [39]. The combination of Equations 3.3-3.7 is the method by which ANSYS solves transient thermal simulations and is the method employed for the remainder of this thesis.

3.3.2 Isolated Heating and Cooling Segments

The four cases in the analytic analysis are simulated in order to verify the quality of future simulations. The 30/10 heating/cooling rate is examined. The temperature differential is the same for the remaining rates and the difference in heat flux profile between them is assumed to be negligible. It should be noted that in the initial analysis in Section 3.1, the heat flux was calculated for one-dimensional heat flow. The simulated analysis determined the three-dimensional heat flow while data presented represents heat flow in one dimension. Therefore differences in the heat flux values in this analysis are due primarily to diffusion of heat in the angular and axial dimensions.

3.3.2.1 Heating From Skin Temperature

In case 1 the actuator increases from skin temperature, 32°C, one degree to 33°C over a period of ten seconds. In the analytic analysis, an initial heat flux of 0 W/m^2 was followed by a strong linear heat flux profile for the entirety of the heating segment. The analytic analysis showed an initial value of 0 W/m^2 followed by a linear increase to a value of 150 W/m^2.

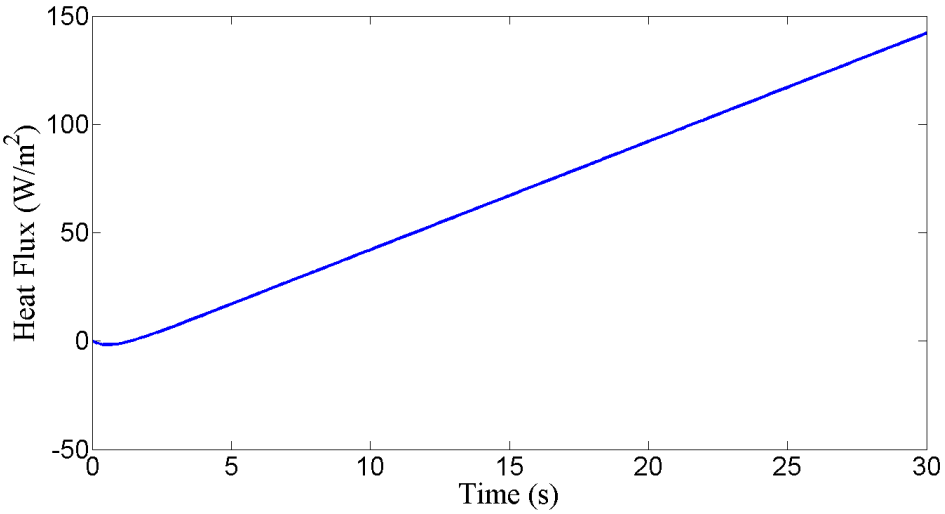

Figure 3.17: Simulated case 1 where the temperature increases one degree over thirty second from 32°C to 33°C. The heat flux increases from 0 W/m^2 to approximately 142 W/m^2.

Initially, there is a slight non-linearity in the heat flux value. This is likely due to the transient heat flow and necessity of heat to propagate into the polyurethane cylinder in order for any amount of flux to be present. Following this transient period, the expected linear profile dominates the heat flow characteristics of the segment. The data shows a final heat flux value of approximately 142 W/m^2. This results in a five percent difference between the analytic and simulation analysis. This is likely due to the heat energy flowing in non-radial directions. Figure 3.17 is consistent with the data shown in the theoretical analysis.

3.3.2.2 Heating From Below Skin Temperature

In case 2 the actuator temperature increases from below skin temperature from 31.5°C to 32.5°C. Initially negative heat flux increases linearly to a symmetric positive heat flux value. The analytic calculations showed an initial negative heat flux value was approximately -75 W/m^2 and the final value was 75 W/m^2.

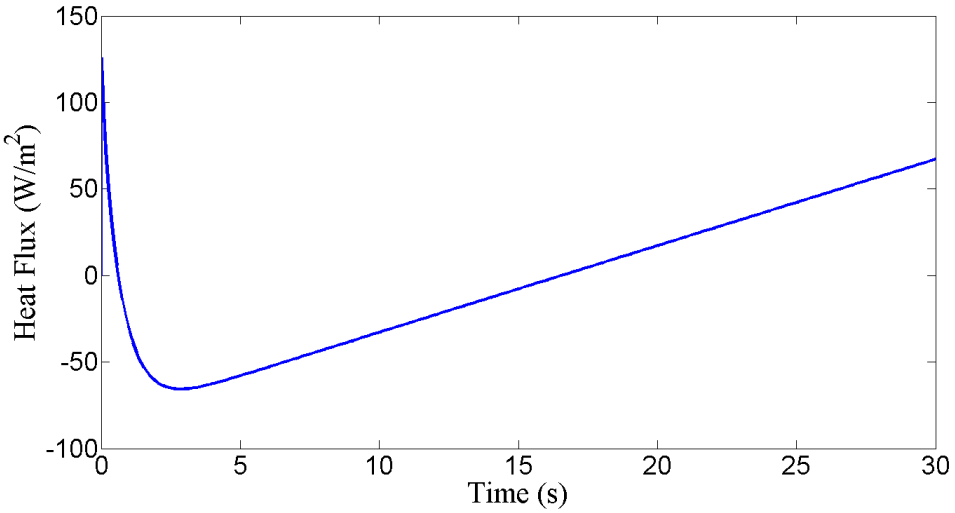

Figure 3.18: Simulated case 2 where the temperature increases one degree over thirty second from 31.5°C to 32.5°C. The heat flux increases from approximately -66 W/m^2 to 67 W/m^2.

An initial non-linearity in the data is present at the beginning of the analysis but it does stabilize within the first five seconds. The observed initial spike in heat flux is likely an artifact of the simulation setup. There is an initial uniform temperature setting required in ANSYS. This was set to 32°C to mimic the steady state temperature of the body assumed to be present prior to heating.

A comparable trend is observed in the heat flux profile compared with the analytic analysis. The heat flux profile is approximately symmetric around zero. However, due to this initial transience, the location of zero heat flux is shifted from the midpoint time of 15 seconds to approximately 16.5 seconds. The heat flux values obtained from the ANSYS simulation were

approximately -66 W/m^2 and 67 W/m^2. The data shows an approximately 12 percent difference for the initial and final values of heat flux compared with the analytic analysis.

3.3.2.3 Cooling From Above Skin Temperature

Case 3 is the first of the cooling scenarios where the initial temperature is at 32.5°C and decreases 1 degree to 31.5°C over ten seconds. The analytic analysis showed a symmetric profile with equal and opposite heat flux values at the beginning and end of the cooling segment. Figure 3.19 is the heat flux profile for this cooling segment.

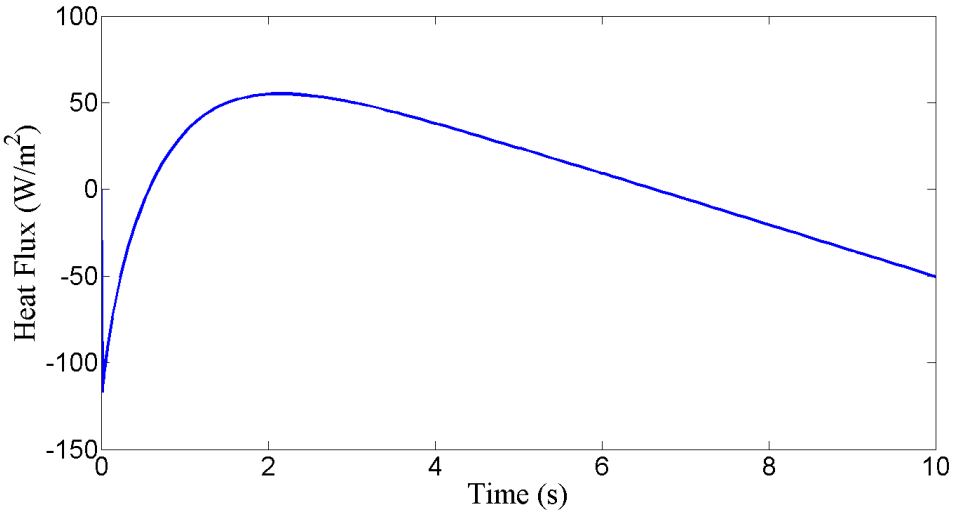

Figure 3.19: Simulated case 3 where the temperature decreases one degree over ten second from 32.5°C to 31.5°C. The heat flux decreases from approximately 55 W/m^2 to -51 W/m^2.

In this case a trend similar to case 2 was observed with a slight non-linearity at the beginning and relative stability reached shortly after as well as some level of symmetry around zero. The initial transience at the beginning of the simulation shifted the location where the heat flux becomes 0 W/m^2 from five seconds to approximately 6.64 seconds. The heat flux values produced by ANSYS are approximately 55 W/m^2 and decrease to approximately 51 W/m^2. This leads to a 26 percent difference from the analytic analysis. This discrepancy is likely due to the increased rate of temperature change. The analytic case assumed a uniform temperature propagation, however, the speed of cooling may have allowed less heat to leave the system.

3.3.2.4 Cooling From Skin Temperature

Case 4 is the final cooling scenario where the temperature cools one degree from 32°C to 31°C over ten seconds. An initial value of 0 W/m^2 with a linear decrease to -150 W/m^2 was observed in the analytic case.

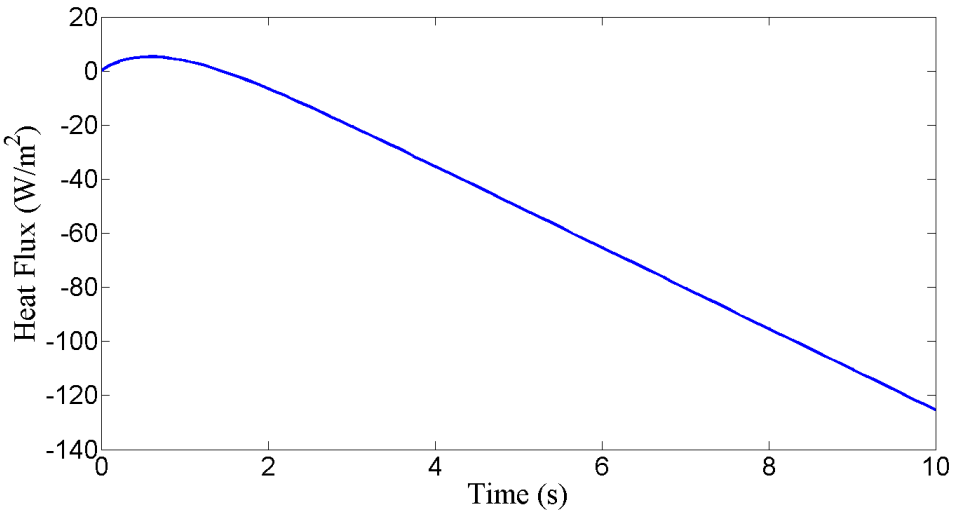

Figure 3.20: Simulated case 4 where the temperature decreases one degree over ten second from 32°C to 31°C. The heat flux decreases from approximately 0 W/m^2 to -125 W/m^2.

Case 4 shows the expected negative heat flux trend. As with the all the simulated cases, a slight non-linearity is present at the beginning of the simulation. This gives way to the expected highly linear heat flux profile for the remainder of the simulation. The initial heat flux value produced is 0 W/m^2 and the final value is approximately -125 W/m^2. This resulted in a 16 percent difference between the analytic and simulation analysis. The cooling segment takes place over a shorter period of time and therefore it is likely that the error between the two analyses is the resultant of less heat being removed from the system.

3.4 Asymmetric Heating and Cooling Cycles

The human skin contains specific sensors called thermoreceptors which respond to heating and cooling thermal stimuli. Skin temperature patterns over the body are directly associated with

specific emotional responses. Temperature perception is directly related to the rate of temperature change and hot receptors respond much slower than cold receptors [6]. Under this principle, it was hypothesized that using an array of thermal actuators oscillating between two temperatures, a perception of constant cooling could be achieved without affecting the average temperature of the skin. The heating actuators increase at a rate below the thermal threshold and the cooling actuators decrease temperature at a rate above the perceivable threshold. Multiple heating and cooling rates were examined in order to observe the affects of different timing patterns. Additionally, several unique spatial patterns were investigated. The heat flux characteristics associated with several asymmetric heating and cooling cycles is discussed.

Two different sections of the cylinder model are examined for this section of the study. The first is along the centerline, under and between two actuators defined in Figure 3.21. The second is along the centerline, under and between all four actuators of the cylinder along the z-axis. For this section of the study, the first actuator will be referred to as "first actuator" and the second actuator along the z-axis will be referred to as "second actuator" as described in Figure 3.21.

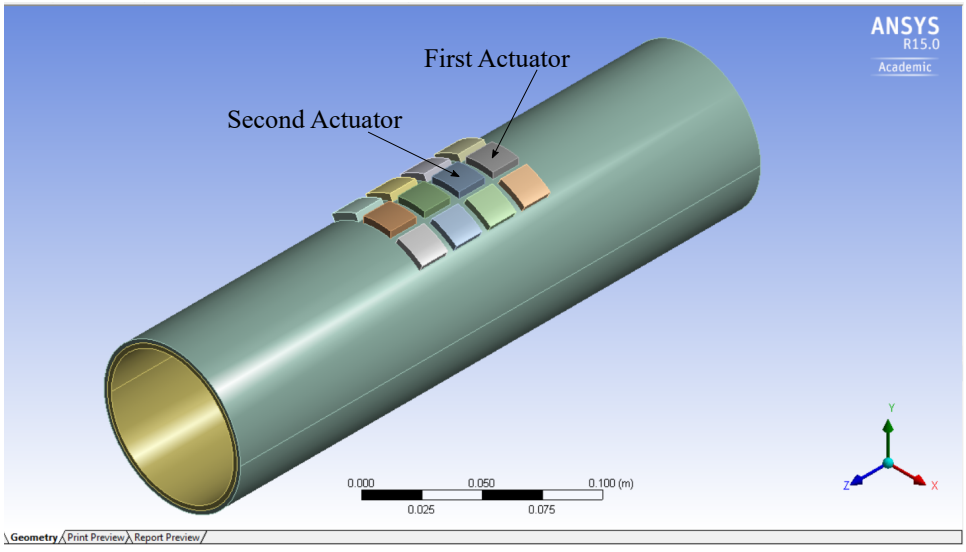

Figure 3.21: Global coordinate system orientation and actuator names. The global orientation of the cylinder is defined. Names for the actuators of interest in this study are listed and will be used for the remainder of this section.

For this simulation, the y-axis represents the radial direction, the z-axis represents the axial direction and the x-axis represents the angular direction. These are directly related because the probe represents a singular point location and therefore, most significantly for the x-axis, can be seen as a value exactly tangential at the centerline. That is, at the centerline the cylindrical value is equal to the Cartesian value. This only hold true at the centerline which is seen to be the middle row of four actuators.

3.4.1 Temporal Patterns and Spatial Patterns

The three primary timing and spatial patterns that were tested, and evaluated were chosen based on limitations and requirements of the physical system. The setup of the original experiment determined the ratio of timing patterns. There are four rows of three adjacent actuators; one row is at its peak value of 32.5°C, one row is at its minimum value of 31.5°C and two rows are slowly heating. This leads to a ratio of 3/1 heating/cooling. All timing patterns chosen for simulation are scaled based on this ratio. The three timing patterns are 21/7 heating/cooling (0.047 °C/s and 0.14 °C/s), 30/10 heating/cooling (0.033 °C/s and 0.1 °C/s) and 45/15 heating/cooling (0.022 °C/s and 0.067 °C/s). All timing patterns meet the requirement of being below the threshold rate for heating and above the threshold rate for cooling.

The three spatial patterns selected for simulation are horizontal, diagonal and arbitrary. The horizontal pattern is defined as a row of three neighboring actuators at the same location along the z-axis. As one row of actuators reaches its peak and begins cooling, the following row of actuators begins heating. The diagonal pattern is defined as three adjacent actuators in different rows along the z-axis. The corner of each actuator is in contact with the adjacent actuator corner. The arbitrary pattern consists of two actuators in the same row on either side of the centerline and one actuator on the centerline two rows ahead. Visually this can be equated to the vertices of an isosceles triangle. All of these patterns shift along the positive z axis until the fourth row of actuators is reached at which point, the pattern was started again at the first row of actuators.

To better understand of what is actually being examined, it is necessary to investigate the general heat flow patterns generated by the different combinations of spatial and temporal patterns used in the experimental setup. The first two actuators along the centerline are examined in depth initially and it is the heat flow in the area under and between that is discussed. For simplicity, the 30/10 heating/cooling pattern will be discussed in detail because the different timing patterns are independent of the spatial patterns. As such, this explanation will hold for the 21/7 and 45/15 heating/cooling patterns as well.

The arrows in Figure 3.22 represent when the first and second actuators reach their respective peak values, 32.5°C, over the course of one heating/cooling cycle. The base of each arrow represents the first actuator while the tip of each arrow represents the second actuator. Figure 3.22(a) represents the horizontal pattern where the first (arrow base) and second (arrow tip) actuators are heating and cooling at the beginning of the cycle. Figure 3.22(b1) and (b2) represent the diagonal pattern. Figure 3.22(b1) shows that for one cycle, the first actuator will begin heating after the second actuator. However, after the first actual cycle, the order of the first two actuators heating/cooling follows the same order and the other patterns (Figure 3.22(b2)). Figure 3.22(c) displays the heating/cooling time for the arbitrary pattern. At any time in the cycle, the first actuator will begin heating prior to the second actuator and this order of actuation will continue throughout the simulation. It is assumed that at steady state, the same heat flow behavior exists at all locations between any two actuators. The general heat flow characteristics for the three patterns is described.

3.4.1.1 Horizontal

At the beginning of this test, the first row of actuators begins heating from 31.5°C to 32.5°C while the subsequent rows are maintained at 31.5°C. This means that heat will begin to flow from the heating actuator to the stagnant actuators. After ten seconds, the adjacent row begins to heat at the same rate as the previous row. This pattern continues for the duration of the simulation.

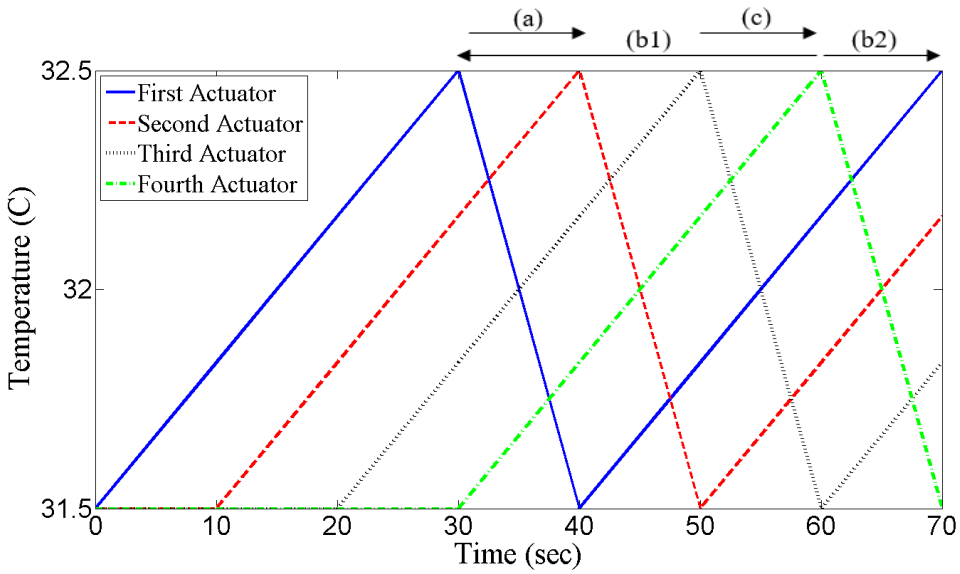

Figure 3.22: One cycle of 30/10 heating and cooling cycle. (a) represents the horizontal pattern where the first and second actuator reach peak values first. (b1) represents the diagonal pattern where the second actuator reaches peak value at the beginning of the cycle while the first actuator reaches its peak at the end of the cycle. (b2) represents the diagonal pattern after the initial cycle is completed. (c) represents the arbitrary heating pattern where the first and second actuator reaches peak values at the end of heat cycle.

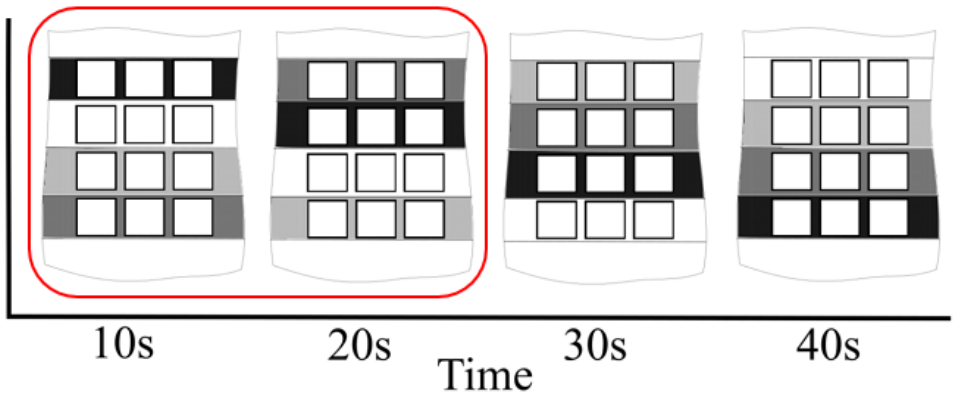

Figure 3.23: The horizontal heating pattern. The peak temperatures (black) for the area of interest in this study is circled in red. 2016 IEEE [8]

For the first 30 seconds, heat is moving in the direction of the second actuator (positive z-axis, as defined in Figure 3.21. At 30 seconds, the first actuator begins to cool rapidly causing heat to move more slowly in the same direction. After approximately three seconds, the second actuator

will be at a higher temperature and the heat will begin flowing in the opposite direction. Refer to Figure 3.22(a) for the temperature differential profile of these actuators. For the horizontal pattern, the heat flux along the x-axis should be relatively negligible because the actuators along the x-axis are all heating and cooling at the same rate leading to no temperature differential and therefore no heat flux. The y-direction should experience large heat flux values underneath the actuators and smaller but still significant heat flux values between the actuators.

3.4.1.2 Diagonal

Diagonal rows of actuators are heated and cooled in groups of three. The first two diagonal sections of actuators consist of three corner touching actuators. The third and fourth sections of diagonal rows overlap the ends of the actuator field. That is, with two corner touching actuators and a single actuator at the opposite end.

As seen in Figure 3.24, the second actuator begins heating first. This is the opposite of the horizontal and arbitrary pattern. However, after the initial cycle of heating and cooling, the heating pattern can be observed as the same type of heating pattern when looking at the first two actuators where the first actuator heats and cooler prior to the second actuator (this is only applicable after the initial transient heating section). This is illustrated in Figures 3.22(b1) and 3.22(b2).

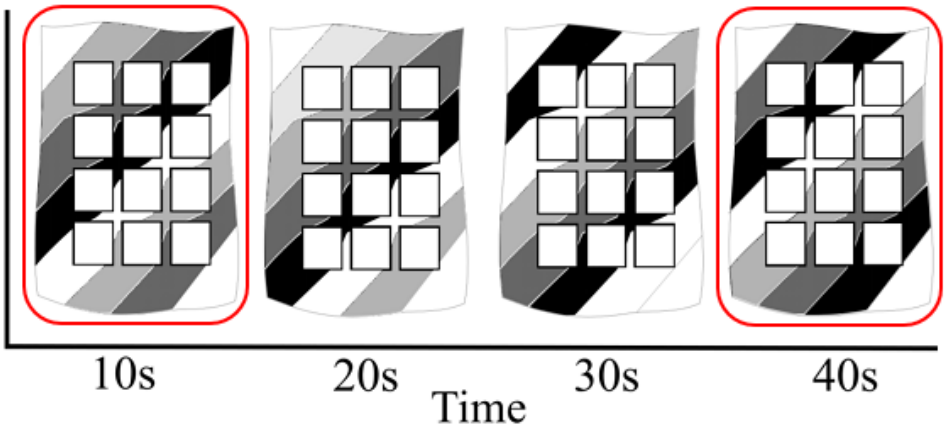

Figure 3.24: The diagonal heating pattern. The peak temperatures (black) for the area of interest in this study is circled in red. 2016 IEEE [8]

The diagonal pattern sees different heat flow patterns in the x direction. For the actuators parallel to the x-axis, the actuators are not heated at the same time and therefore heat is flowing more noticeably. For the two central heating modes, little temperature change is in the domain of the centerline and therefore, little heat flux exists (Figure 3.24 20s and 30s). The z-axis heat flux remains relatively unchanged and after the initial heating cycle is viewed as identical to the horizontal pattern. The y-axis heat flux is also unchanged as the direction of changing actuators is orthogonal to the y-axis.

3.4.1.3 Arbitrary

The final primary heating pattern is the arbitrary pattern. This pattern is described as three non-touching actuators heating at the same time. In this pattern, two actuators are in line with the x-axis while the third is two rows ahead of the two other actuators. (vertices of an isosceles triangle). After the delayed period of heating, a new group of three non-touching actuators begins heating. This pattern continues for the duration of the simulation. The area of interest for this study does not reach peak values until the end of each heating cycle.

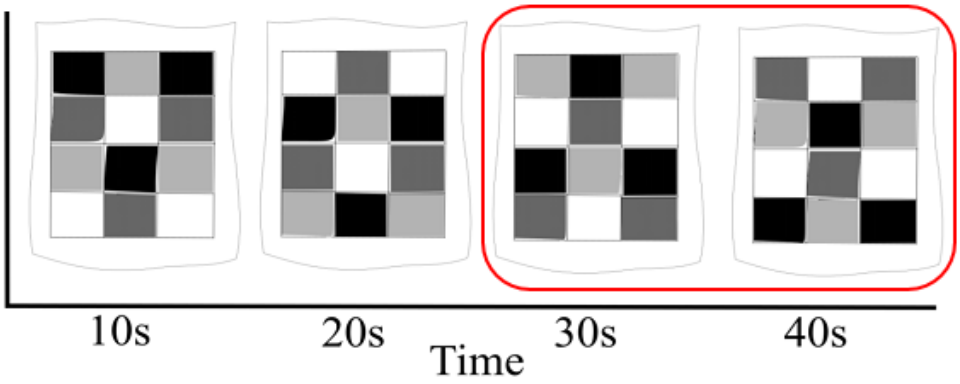

Figure 3.25: The arbitrary heating pattern. The peak temperatures (black) for the area of interest in this study is circled in red. 2016 IEEE [8]

This pattern affects the x-axis and z-axis heat flux more significantly than in the previous heating patterns. In the first rows of actuators, heat is diffused toward the centerline of the area of interest. The heat capacity of the skin will allow for storage of some additional heat that is

not present in the other patterns. The z-axis heat flux for the first two rows reduces because no heating is taking place between the two center actuators at the beginning of the heating cycle. In the second half of one cycle, the two center actuators are heating in a way that is identical to the previous patterns. However, due to some heat storage from earlier in the heating cycle, different values for heat flux in the z direction may be present compared with the other patterns. The temperature may be slightly raised due to the heat storage and therefore smaller temperature differentials will be present causing lower heat flux values.

3.4.1.4 Simulated Patterns

Based on the time patterns and spatial patterns, nine different simulation combinations were performed. Horizontal 21/7, 30/10 and 45/15, diagonal 21/7, 30/10 and 45/15, and arbitrary 21/7, 30/10 and 45/15 are the nine pattern combinations chosen to be simulated. It should be noted that not all nine combinations were tested experimentally; five of the nine were testes. The three rates were tested in combination with the diagonal pattern and all three spatial patterns were tested with the 30/10 heating/cooling rate. Rates that were not tested include: Horizontal and Arbitrary at both 21/7 and 45/15.

The thermal patterns, listed above, were simulated and the heat flux and temperature values were collected and analyzed. The time delay of each actuator segment at the beginning of the simulation causes a transient state of heat transfer. In order to eliminate any transient effects, the first 90 time step values were removed from analysis. This resulted in a total analysis time of one minute and eight seconds for the 21/7 rate, one minute and 36 seconds for 30/10 and two minutes and 25 seconds for the 45/15 rate.

3.4.2 Heat Flux Profile for Two Actuators

For this section of the thesis, five discrete points are analyzed. Capabilities in ANSYS allow for physical quantities to be calculated and displayed at discrete locations at any point on a simulated model. These locations are referred to as “Probes” and quantities such as heat flux and

temperature can be calculated in ANSYS transient thermal analysis. Additionally, multiple probes can be placed in the same location in order to measure different quantities at the same location. In this section of the study, five probe locations have been selected for analysis. Figure 3.26 shows the locations of the five heat flux and five temperature probes. Probe locations one and five are directly under the center of the first and second actuators. Probes two, three and four are between the first and second actuators. Two and four are located one millimeter from the edge their adjacent actuator. Probe three is located directly at the midpoint between the first two actuators.

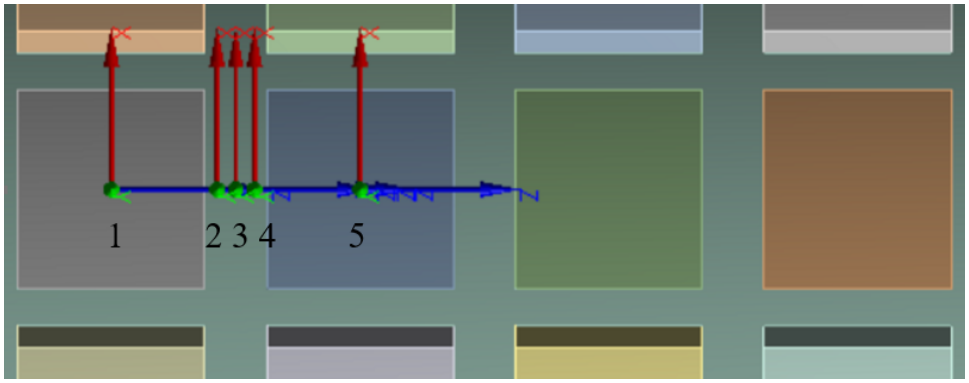

Figure 3.26: Probe locations under and between first two actuators. The five locations where heat flux data was examined for this analysis.

Here, the global minimum and maximum values of heat flux in the x, y and z direction and the total magnitude for each probe location (Figure 3.26) are measured, excluding initial transience (the first cycle of heating/cooling), and the difference is taken. The heat flux difference profile for each direction is plotted based on the specific time pattern. For each set of data below, the spatial pattern is held constant. The heat flux difference values in the x-direction are significantly lower than the other directions and do not exhibit substantial changes. Therefore, the x-direction values will not be heavily investigated.

The first group to be examined is the horizontal heating pattern. Table 3.4 shows that at locations one and five, which represent the probes directly under the actuators, take the largest value in the y direction. This is reasonable because those areas are in closest contact with the changing temperatures and therefore experience the largest positive and largest negative heat flux

values leading to the largest heat flux difference values. The heat flux values in the x and z direction for probes one and five have the smallest heat flux difference values. This is because the area surrounding the probes experience very small temperature differential and therefore very little change in heat flux.

Table 3.4: Heat flux difference values for the horizontal pattern. Data for x, y and z directions as well as the total magnitude for all five probe locations is shown.

Horizontal 21/7 (W/m^2)					
Probe	1	2	3	4	5
Diff-x	0.78	0.45	0.43	0.47	0.44
Diff-y	134.7	30.7	8.7	32.0	142.4
Diff-z	0.8	36.2	15.5	28.5	0.2
Diff-Total	68.3	23.9	7.2	22.9	74.1
Horizontal 30/10 (W/m^2)					
Probe	1	2	3	4	5
Diff-x	0.57	0.35	0.39	0.37	0.29
Diff-y	139.1	34.1	10.8	37.3	144.6
Diff-z	0.6	39.2	17.4	30.0	0.1
Diff-Total	71.9	24.9	8.0	25.1	74.2
Horizontal 45/15 (W/m^2)					
Probe	1	2	3	4	5
Diff-x	0.40	0.32	0.36	0.28	0.20
Diff-y	142.0	38.3	14.1	42.8	146.2
Diff-z	0.4	41.2	19.1	31.5	0.1
Diff-Total	70.5	25.9	8.5	27.7	73.8

Probes two and four, located 1mm from the edge of the first two actuators, experience heat flux difference values that exhibit entirely different characteristics when compared with probes one and five. The heat flux difference values in the y direction, while still significant, are much smaller than those underneath the actuators. The y-direction values are smaller because the temperature difference, in the y-direction, is not as large due to distance from the heating source. The temperature differential in the x and z direction is much larger because the surrounding area is not subjected to the same amount of heat (compared to the area directly under the actuator). Because of the temperature differential, heat is diffused in the x and z direction, primarily the z-direction, and is the cause for larger heat flux difference values in the z direction. The heat flux difference in z increased by approximately 45 times from probe one to two and probe five to four for the 21/7

rate and by nearly 100 times for the 45/15 rate. The slower rate causes a larger heat flux difference along the centerline which may decrease the cooling perception by confusing the thermoreceptors, similar to the thermal grill, without stimulating nocioceptors. Additionally, the heat flux values in the y and z direction, at probes two and four, are all very similar. At probe two, the heat flux difference value between the y and z direction is 8 percent for 21/7, 10 percent for 30/10 and 14 percent for 45/15. The heat flux difference values at probe four are slightly larger at 37 percent 21/7, 39 percent for 30/10 and 41 percent for 45/15.

The heat flux difference values are significantly lower at probe three for all directions when compared with probes two and four. It is also noticeable that at this distance, 2.5mm between actuators, the heat flux difference in the z direction is the dominate heat flow direction. This seems to indicate a parabolic heat flow pattern between actuators. 2.5mm is the furthest possible distance from the heating source and therefore experienced a significantly lower temperature differential in the y-direction than in the z-direction. Heat flow in the y direction is reduced by as much as 72 percent between probe 2 and probe 3 for the 21/7 heating/cooling rate. Figure 3.27 shows the heat flux profiles for the horizontal pattern at the three primary rates. These plots correspond with the data in Table 3.4.

Identical simulations were run for the remaining patterns. The same analysis was performed where the global minimum and maximum values of heat flux were found and the differences calculated. There was very little change in the heat flux difference profiles for the diagonal and arbitrary patterns. The diagonal pattern for all timings is discussed followed by the arbitrary patterns for all timings.

From Table 3.5 it is seen that for all three time rates in combination with the diagonal spatial pattern, the heat flux differences are approximately the same as the horizontal pattern. The differences for the heat flux difference values in the y direction change less than one W/m^2 for probes one, two and three; the remaining probes did not change in the y-direction. The value at the third probe location increases minimally while the values at each end (probes directly under the actuator) decrease slightly when comparing the diagonal pattern to the horizontal pattern. This

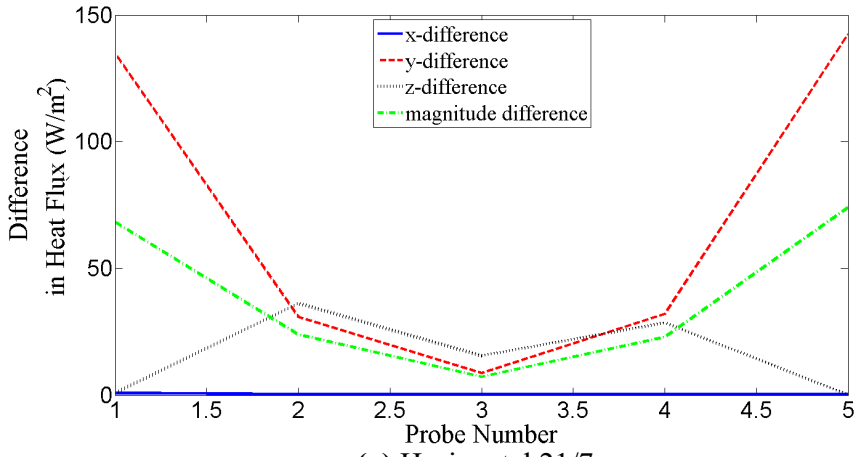

(a) Horizontal 21/7

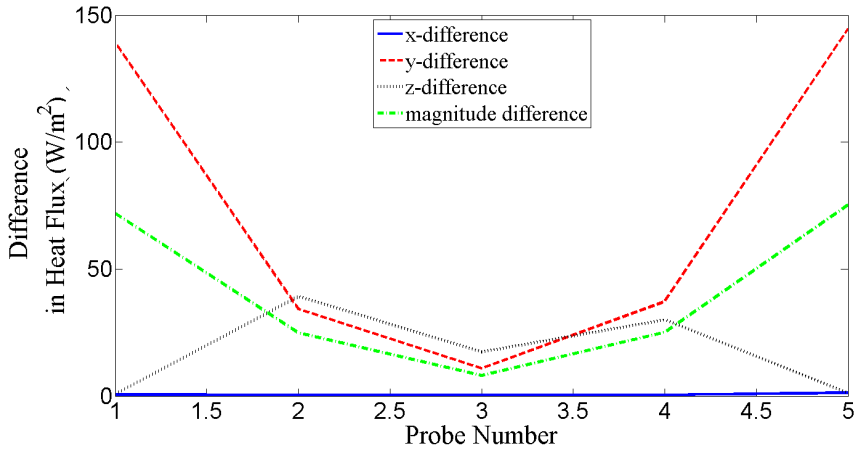

(b) Horizontal 30/10

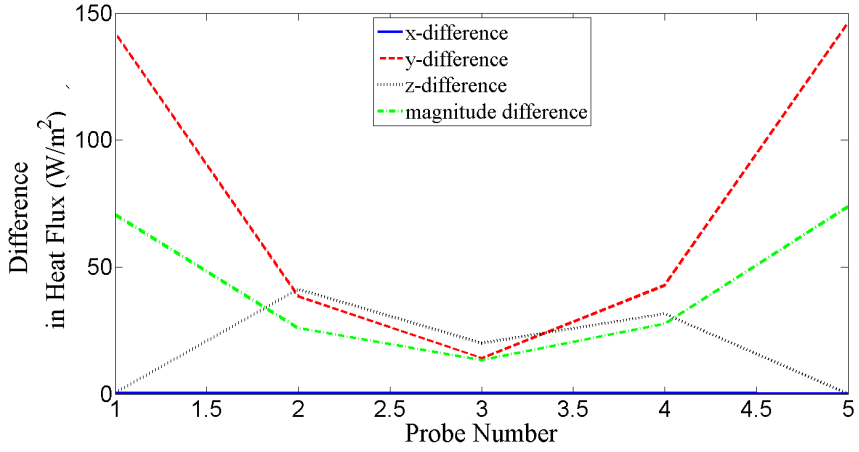

(c) Horizontal 45/15

Figure 3.27: Heat flux profile for horizontal simulation patterns. (a) is Horizontal 21/7. (b) is Horizontal 30/10. (c) is Horizontal 45/15.

Table 3.5: Heat flux difference values for the diagonal pattern. Data for x, y and z directions as well as the total magnitude for all five probe locations is shown.

Diagonal 21/7 (W/m^2)					
Probe	1	2	3	4	5
Diff-x	0.81	0.41	0.43	0.47	0.43
Diff-y	134.8	30.9	8.8	32.0	142.4
Diff-z	0.9	36.2	15.6	28.7	0.2
Diff-Total	68.3	23.9	7.2	23.0	74.1
Diagonal 30/10 (W/m^2)					
Probe	1	2	3	4	5
Diff-x	0.56	0.35	0.39	0.38	0.28
Diff-y	139.1	34.2	10.9	37.3	144.6
Diff-z	0.6	39.2	17.4	30.1	0.1
Diff-Total	71.9	24.9	8.0	25.2	74.2
Diagonal 45/15 (W/m^2)					
Probe	1	2	3	4	5
Diff-x	0.38	0.32	0.36	0.28	0.20
Diff-y	142.0	38.2	14.1	42.8	146.2
Diff-z	0.4	41.2	19.1	31.5	0.1
Diff-Total	70.5	25.9	8.5	27.7	73.8

ultimately leads to a smaller slope between the probe locations. This could indicate more even thermal sensation but does not mark a relationship with thermal perception magnitude.

From Table 3.6 it is seen that for all three time patterns in combination with the arbitrary spatial pattern, the heat flux profile is approximately the same as both the horizontal and diagonal pattern with minor variations for the inner probe locations. The values at locations one and five represent the heat flux difference for the probes directly under the actuators at a depth of one millimeter into the skin. Locations two, three and four show the values for the probes between the actuators at a depth of one millimeter into the skin.

The directional heat flux under the actuators is dominated by heat flow in the y-direction which is consistent with the other patterns. The probe locations under the actuators are directly under the center of the actuator causing the temperature differential in the y-direction to much larger than the temperature differential in either the x or z direction. Comparing all the values in Tables 3.4, 3.5 and 3.6 it is seen that no value at the same location and in the same direction

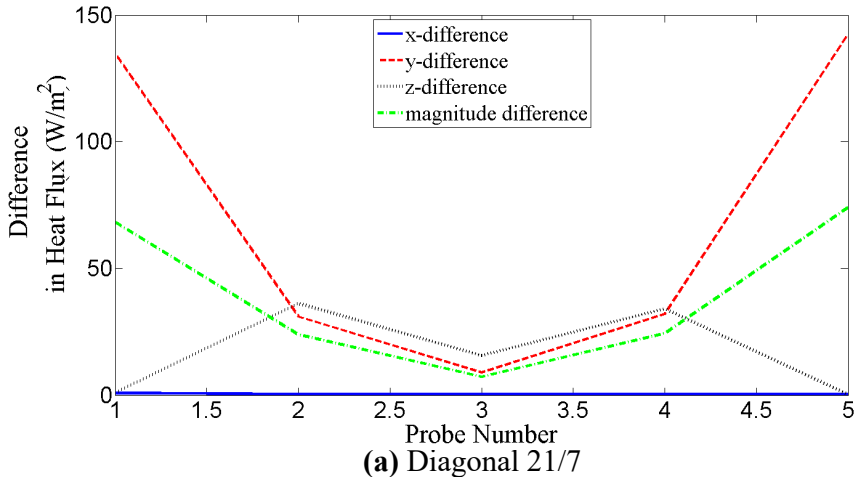

(a) Diagonal 21/7

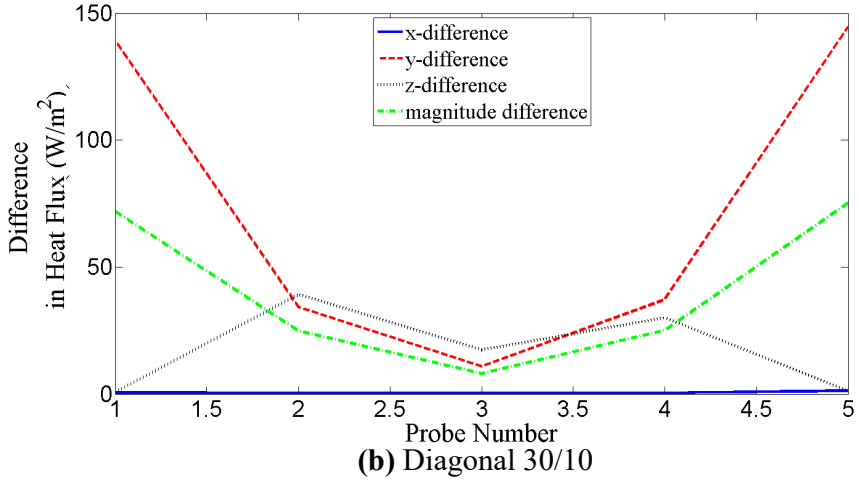

(b) Diagonal 30/10

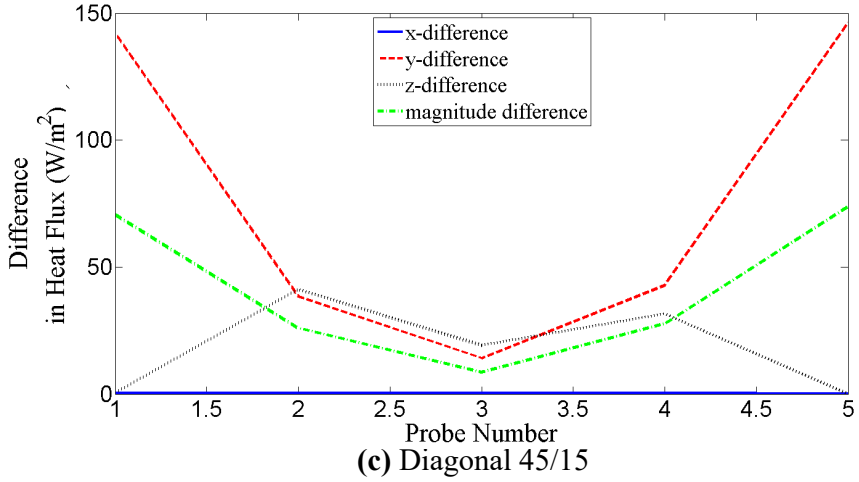

(c) Diagonal 45/15

Figure 3.28: Heat flux profile for diagonal simulation patterns. (a) Diagonal 21/7. (b) Diagonal 30/10. (c) Diagonal 45/15.

Table 3.6: Heat flux difference values for the arbitrary pattern. Data for x, y and z directions as well as the total magnitude for all five probe locations is shown.

Arbitrary 21/7 (W/m^2)					
Probe	1	2	3	4	5
Diff-x	0.80	0.44	0.43	0.48	0.44
Diff-y	134.8	31.2	9.0	32.2	142.9
Diff-z	0.8	36.9	15.5	29.1	0.2
DIff-Total	68.3	23.9	7.2	23.0	74.1
Arbitrary 30/10 (W/m^2)					
Probe	1	2	3	4	5
Diff-x	0.55	0.35	0.39	0.38	0.28
Diff-y	139.1	34.3	10.9	37.4	144.6
Diff-z	0.6	39.2	17.4	30.0	0.1
Diff-Total	71.9	24.9	8.0	25.2	74.2
Arbitrary 45/15 (W/m^2)					
Probe	1	2	3	4	5
Diff-x	0.40	0.33	0.37	0.30	0.19
Diff-y	142.0	38.3	14.1	42.9	146.2
Diff-z	0.4	41.2	19.2	31.5	0.1
Diff-Total	70.5	25.9	8.5	27.8	73.8

changes by more than 0.2 W/m^2. The largest changes in heat flux difference are associated with the changing heating/cooling rates and not with the spatial pattern.

In the three plots in Figures 3.27, 3.28 and 3.29, it is seen that there are some minor differences across all plots. Because the differences are so minor it seems to imply that regardless of what pattern is chosen, the heat flux profile is constant. This also implies that the sensation of constant cooling may not depend strongly on the spatial pattern of actuation. Further examination of the heat flux profile along the centerline of the thermal display will serve to validate the initial assumption that heat flow pattern between actuators is constant after the transient effects are accounted for. Examining the entire centerline of the thermal display, under and between all actuators, will allow for a more thorough evaluation of the entire heat flux profile generated by the temporal and spatial pattern combinations.

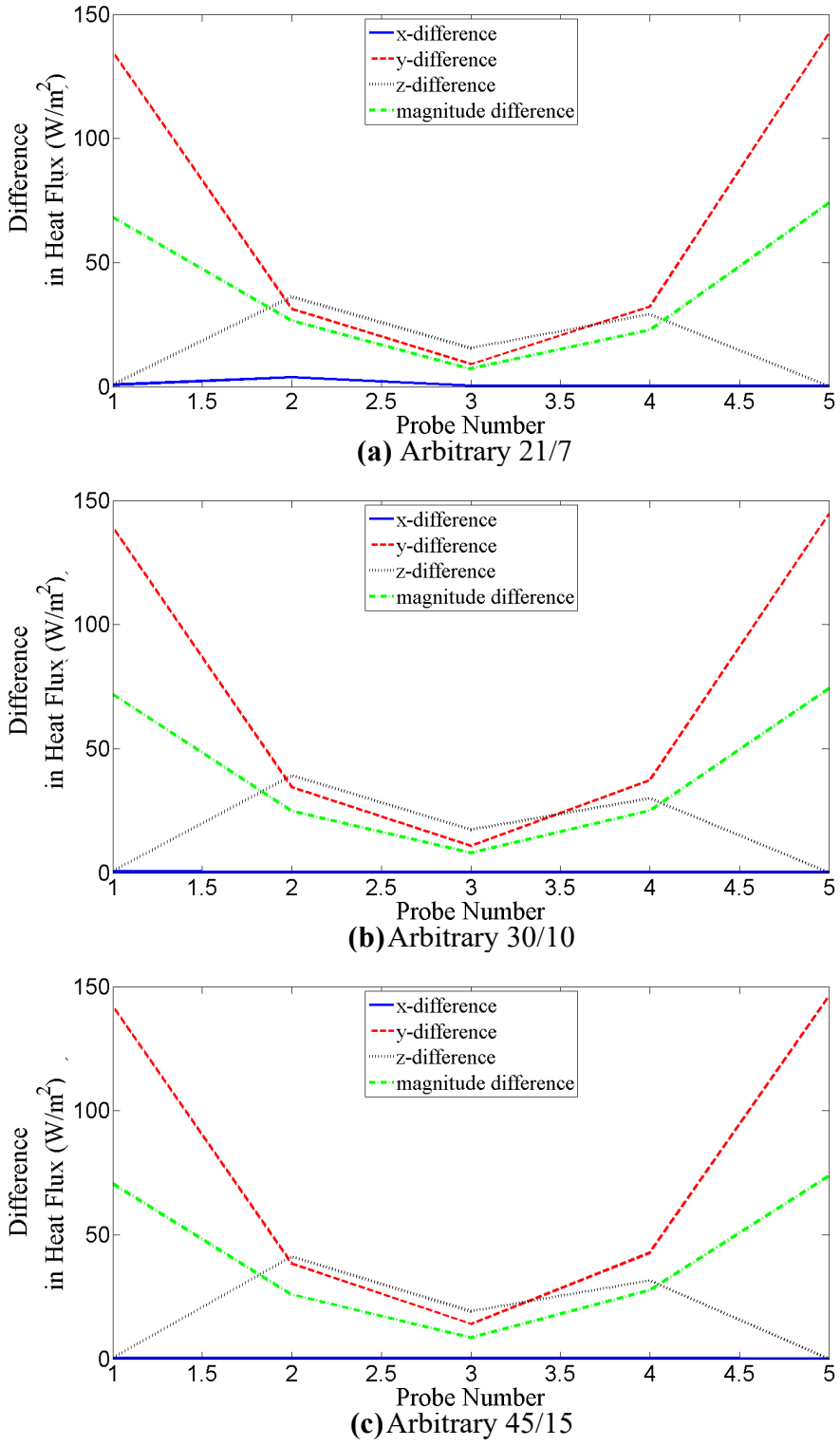

Figure 3.29: Heat flux profile for arbitrary simulation patterns. (a) Arbitrary 21/7. (b) Arbitrary 30/10. (c) Arbitrary 45/15.

3.4.3 Heat Flux Profile for Four Actuators

The study of the heat flux profile of the thermal display is extended along the entire centerline of the thermal device. In the previous examination, one probe was placed under an actuator at two locations (first and second probe) and three probes were placed between these two actuators. This allowed for higher resolution of the heat flux profile between actuators. The assumption is that after an initial transient period, the heat flux profile is nearly constant at all inter-actuator locations. Here, one heat flux probe is placed directly under the center of all four actuators, and one probe is placed directly at the midpoint between each actuator (Figure 3.30). The purpose of this section is to further verify that the heat flux profile along the centerline of the actuators is consistent under and between all actuators. The same method of examination is used to evaluate the heat flux profile along the entire centerline of the model. The global maximum and minimum values of heat flux for each probe location is determined, excluding the initial transient section (first cycle of heating/cooling). The difference between these two heat flux values is calculated as the heat flux difference value. The heat flux difference values are plotted relative to their corresponding probe number. In this section of the study, the odd numbered probes represent the location under the actuators and the even numbered probes are located at the midpoint between actuators. For clarity, it should be noted that probe number two in this section is equivalent to probe number three from the previous section and that probe number three in this section is equivalent to probe number five in the previous section.

In the previous section, it was observed that the differences in the heat flux profile for the different patterns was negligible. Additionally, the different timing rates only scaled the heat flux profile for each spatial pattern by the same magnitudes. Therefore, for the remainder of this study, only the 30/10 heating/cooling rate will be examined.

Looking at the plots in Figure 3.31 an important pattern emerges immediately. The same heat flux profile exists between all actuators along the centerline. This is significant because it justifies the initial assumption that, at steady state, the same heat flow characteristics are present at

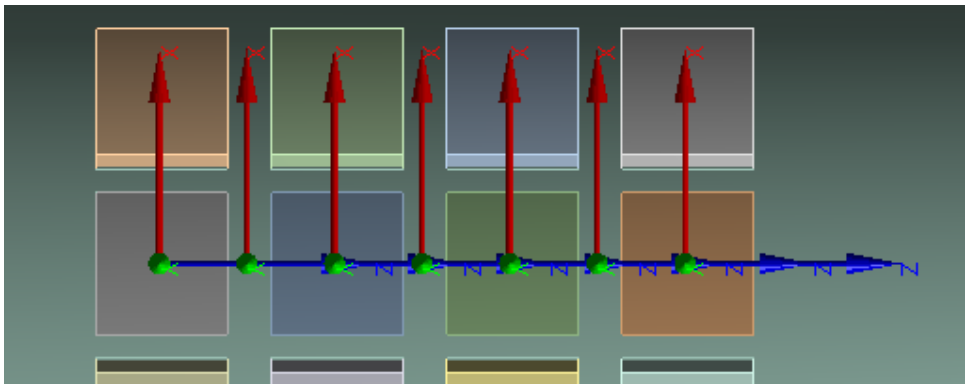

Figure 3.30: Probe locations for four actuator study. The probe locations under and between all four actuators allows for an extended look at the heat flux profile along the centerline of the model.

all inter-actuator locations. Additionally, this assumption was correct for all patterns and was not an artifact of observing an isolated area.

Observing large scale visual trends in the data from Figure 3.31, the most obvious can be seen at probes two, four and six, located between actuators, specifically in the y and z directions. The general trend describes the heat flux difference in the y-direction, as probe number increases, increasing in magnitude for the horizontal pattern, remaining approximately the same for the diagonal pattern and decreasing in magnitude for the arbitrary pattern. In the previous section the diagonal pattern exhibited similar consistency between probe locations. However, it is possible that the larger change in heat flux difference magnitude along the centerline may increase thermal perception. The final visual trend in the date is specific to probe location three in the y direction. The heat flux difference value take its maximum global magnitude at this location for all patterns. The heat flux difference is approximately 4.6 percent larger at this location in the y-direction when compared to the other probes under actuators.

Numerically, the horizontal and arbitrary patterns produced the largest heat flux difference values. The horizontal pattern generated heat flux differences in the x and y directions while the arbitrary pattern dominated the z-direction and total magnitude heat flux differences. The x-direction heat flux for the horizontal pattern was approximately 3.2 percent larger than the other patterns, however, the value is negligible and less than one W/m^2. The y-direction heat flux

produced by the horizontal pattern took the largest value at 144.59 W/m^2. This is the largest heat flux difference value but is not significantly larger than the other patterns at less than one percent difference. The heat flux difference value produced in the z-direction by the arbitrary pattern was the largest of the three patterns at 17.50 W/m^2 which is less than one percent larger than the remaining patterns. The total magnitude value for heat flux difference is largest for the arbitrary pattern. The arbitrary pattern heat flux difference value is less than one percent larger than the other patterns at 74.22 W/m^2. These values are consistent with the previous statement that the diagonal pattern produced the most consistent heat flux difference pattern. The horizontal and arbitrary patterns produced increasing or decreasing trends in their respective heat flux profiles and the values produced agree with this assertion. Additionally, these results further indicate the relative uniformity of the heat flux profiles produced by all pattern combinations. Therefore, in order to develop a relationship between thermal sensation and heat flux a different approach must be take.

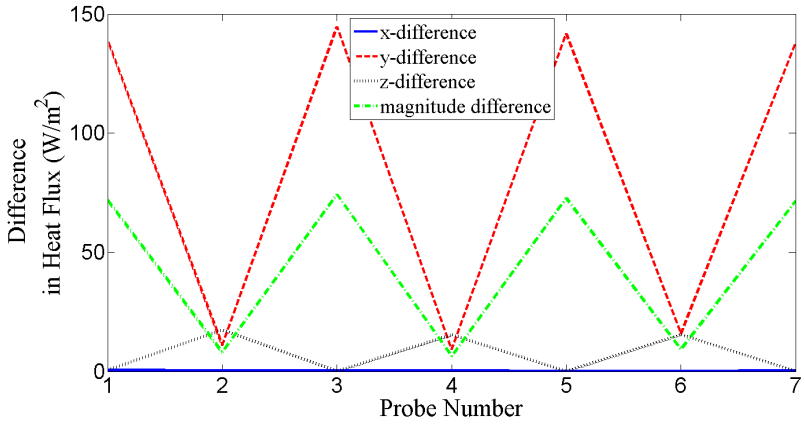

(a) Horizontal 30/10

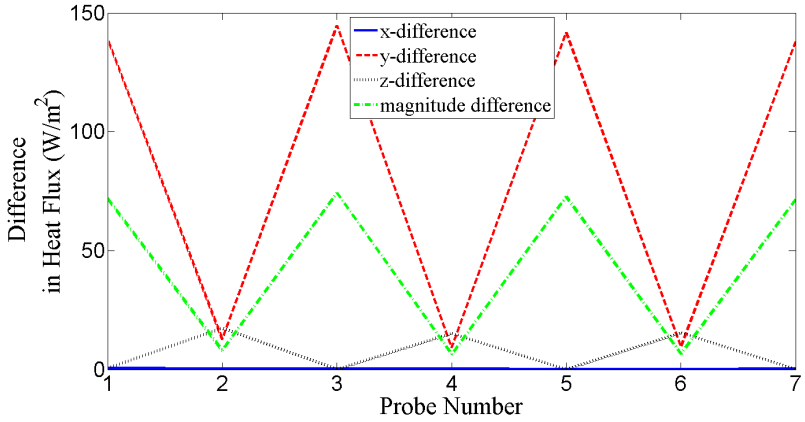

(b) Diagonal 30/10

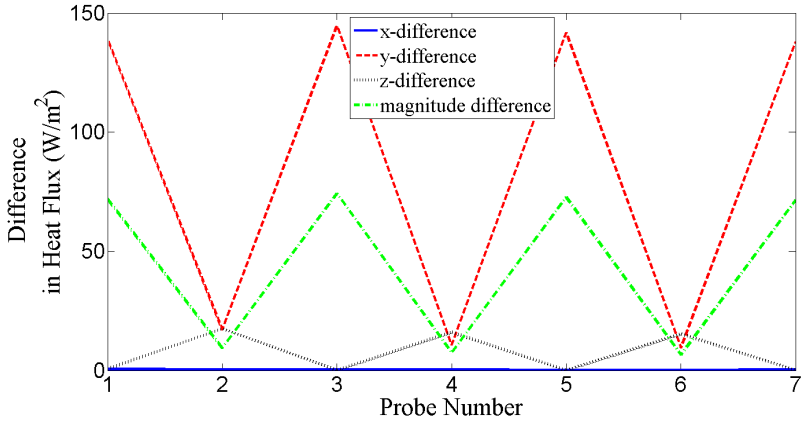

(c) Arbitrary 30/10

Figure 3.31: Heat flux profile for the three spatial patterns at the 30/10 heating and cooling rate. This image is the heat flux profile for the extended centerline of actuators. Odd numbers represent probes under actuators and even numbers represent the probes between actuators. (a) Horizontal 30/10. (b) Diagonal 30/10. (c) Arbitrary 30/10.

3.5 Proposed Correlation Between Experiment and Simulation

The primary goal of this study is to develop a relationship between the thermal perception data garnered from the experiment performed by Manasrah et al. [8] with the heat flux data from the simulations. It is understood that thermal perception is based on the flow of heat through the skin and not the absolute temperature of the skin itself. Heat flow is generated by a temperature differential which causes a heat flux through the skin. For this reason, finding a correlation between the thermal perception and heat flux is desired. A mathematical relationship is proposed that expresses thermal perception as a function of heat flux magnitude, independent of direction. This relationship is a theoretical correlation between the two quantities based on observed trends in both the experimental and simulated data. Additionally, this is a first approximation on the proposed association between perception and flux. This newly proposed relationship will allow for a way to estimate the expected thermal perception based on the various heat flux values obtained from a variety of temporal and spatial patterns. Using this new relationship, simulating new patterns and comparing the heat flux data from each will make it easier to determine the validity and efficiency of each, for future physical experiments.

From the experimental data, thermal perception values were determined based on a slightly altered version of the ASHRAE Standard 55 thermal comfort scale, Table 3.7. ASHRAE Standard 55 ranks thermal perception on a scale from -3 to +3; -3 being cold, 0 being neutral and +3 being hot [41]. Fanger [42, 43] first developed this scale, known as the predicted mean vote, as a method of quantifying an individual's thermal comfort. PMV is determined based on six factors: air temperature, radiant temperature, relative air velocity, vapor pressure of ambient air, metabolic heat rate and thermal resistance of clothing.

Data was taken from a total of 21 participants who were asked questions about their thermal sensation at regular intervals throughout the experiment. The data for each person was quantified using the adjusted ASHRAE standard 55. Means and standard deviations were calculated based on the thermal perception responses from the subjects and quantitative values were determined for the three temporal patterns and the three spatial patterns.

Table 3.7: ASHRAE thermal comfort scale. Thermal comfort is ranked on a scale from -3 to +3 and perception metrics were determined.

Value	Thermal Scale
+3	Hot
+2	Very Warm
+1	Warm
0	Neutral
-1	Cool
-2	Very Cool
-3	Cold

Based on the analyzed data from the physical experiment performed by Manasrah et al. [8], it was determined that for the timing patterns, the 30/10 heating/cooling ratio had the largest mean value of any thermal perception at -0.38. However, this was not statistically different from the 21/7 heating/cooling pattern at -0.33. The 45/15 pattern produced the weakest cooling sensation of the three main timing patterns at -0.19. This is seen in Figure 3.32. Values for the three timing patterns were determined by testing all three at the diagonal spatial pattern.

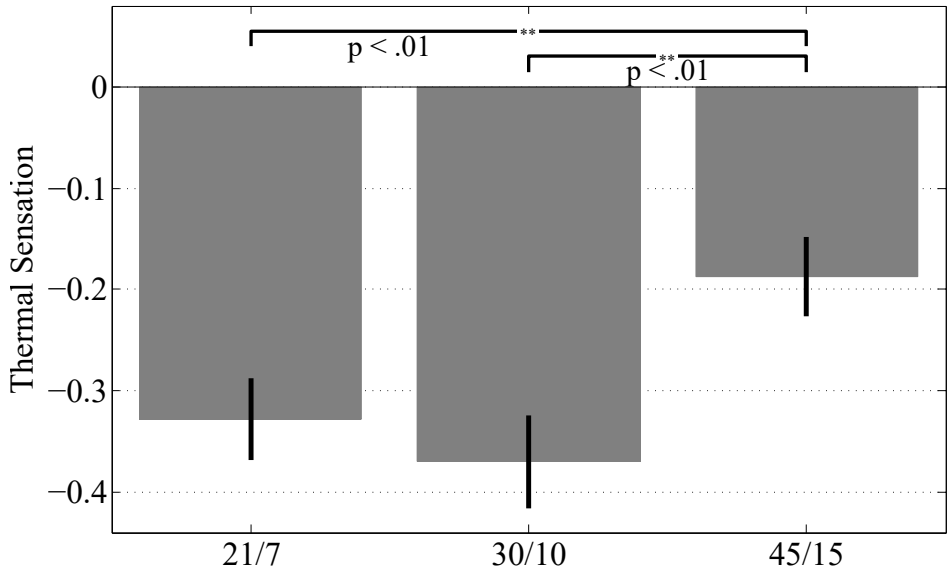

Figure 3.32: Temporal pattern thermal sensation metrics. 30/10 and 21/7 are not significantly different from each other. 45/15 is much less perceivable than the others. 2016 IEEE [8]

From the experimental data for the spatial patterns, it was determined that the horizontal pattern was the most effective with a mean thermal sensation value of -0.53. The mean thermal sensation value for the arbitrary pattern was smaller yet not statistically significantly different from the horizontal pattern at -0.50. The diagonal pattern produced a much lower and statistically different average thermal sensation value of -0.38. All spatial patterns were tested using the 30/10 heating/cooling rate. Figure 3.33 shows the data for all three spatial patterns discussed in this study. There are two additional patterns seen in Figure 3.33, however, diagonal 10/2 and vertical 8/4 were not evaluated for this study. These patterns fell outside the scope of investigation due to their deviation from the standard 3/1 ratios and the different total affected areas. Examining the diagonal, arbitrary and horizontal patterns, which all fit that standard heating/cooling ratio, allowed for a more standardized comparison.

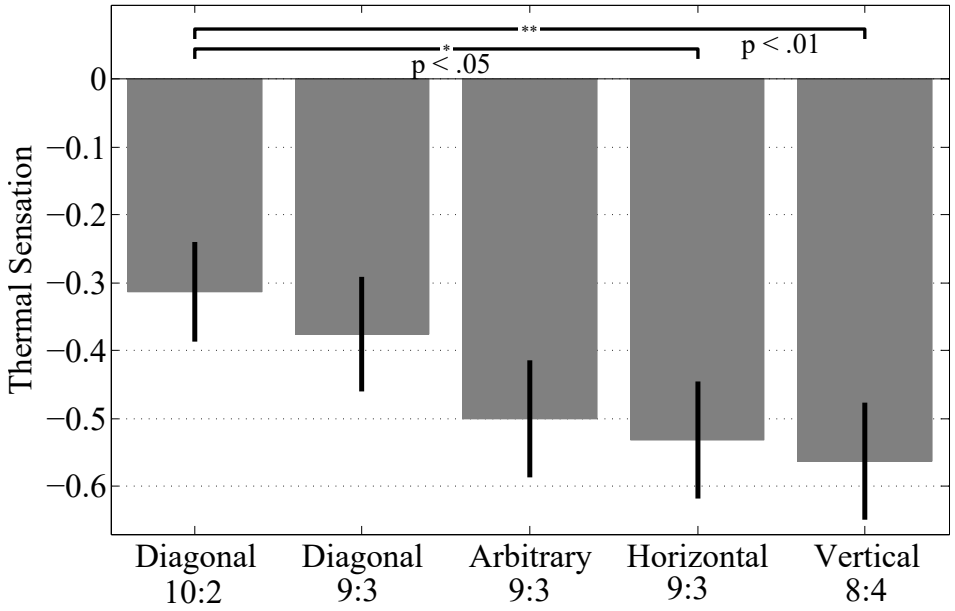

Figure 3.33: Spatial pattern thermal sensation metrics. The horizontal and arbitrary patterns are not significantly different from each other. The diagonal pattern is perceived much less than the others. 2016 IEEE [8]

Initial correlation attempts involved relating the general trends of the actual thermal perception from temporal and spatial patterns generated by Manasrah et al. [8]. Several methods were

employed to try and develop a correlation between thermal perception and heat flux. Trends in the heat flux and temperature profile as well as the actual values were evaluated and compared to the thermal perception of the timing patterns and the spatial patterns individually. The first analysis of the simulated data involved overlaying the heat flux and temperature plots. The goal was to gain some insight on how the maximum and minimum values of temperature were associated with the directional heat flux at any point in time. This was done for each direction (x, y and z) and total magnitude seen through each probe. The results gained from this did not yield a correlation because the global extreme values for heat flux were very similar. Additionally, the same behavior was exhibited by all patterns. For example, The overlain plots of flux and temperature under the actuators were completely in phase with each because the temperature differential in that region was large enough in the y-direction that heat flowed almost exclusively in that direction. The flux and temperature plots for the x and z directions between actuators were out of phase with each other due to the necessity of heat to propagate before a temperature differential could be apparent. This was observed in all patterns and therefore not discernible relationship could be concluded.

The second examination involved identifying differences in the heat flux profile between two and four actuators (Section 3.4.2 and Section 3.4.3). In determining unique differences between each pattern combination, these quantities would be associated with the thermal perception information from the experimental data, Figures 3.32 and 3.33. A range of values were evaluated at all probe locations including: maximum, minimum, average, difference and percent difference. The heat flux profiles for all pattern combinations yielded very similar results. It was observed that regardless of spatial pattern, nearly identical heat flux profiles were generated. Additionally, the different heating/cooling rates served only to scale the different patterns and the scaling was, again, nearly identical between patterns. The intense similarity between patterns made it difficult to recognize any obvious correlations. Valuable information was obtained through this examination, however. For example, the actual heat flux values, not the general trends, used to evaluate the unique profiles of each pattern were ultimately used to develop the theoretical correlation.

To this point, all previous sections attempted to determine a correlation between thermal perception and heat flux by observing trends. Specifically trends between heat flux and temporal perception values (Figure 3.32) *or* heat flux and spatial perception values. However, it was ultimately determined that a combination of both trends was necessary for developing a relationship. A combination of both metrics allowed for each unique pattern to have a unique thermal perception value associated with it. The correlation will be developed and discussed below and serves as a first approximation on the relationship between the thermal perception achieved by the thermal display developed by Manasrah et al. [8], and the heat flux values determined through out the course of this thesis.

3.5.1 Perception Metrics

The thermal perception values listed above were combined in several ways in order to generate a relationship between the patterns. It should be noted that physical experiments for horizontal 21/7, horizontal 45/15, arbitrary 21/7 and arbitrary 45/15 were not performed. Perception metrics for these combinations were extrapolated from the the existing data. For simplicity, the spatial pattern metrics in Figure 3.33 will be denoted as "S" and the temporal pattern metrics in Figure 3.32 will be known as "T". Several combinations of these perception metrics were looked at including multiplication of metrics, inverse combination of metrics, and square roots of metrics; some showed promising trends and potential for a relationship with heat flux.

The theory behind this evaluation was to view each metric as a vector and to perform different mathematic operations on them. Simple metric combinations were tried first. For example, addition and subtraction of the two pattern metrics; $S+T$ and $S-T$ this was done as a simple initial attempt and combining metrics. The inverse values of both of these were calculated, $1/(S+T)$ and $1/(S-T)$. More involved metrics were evaluated, for example, the ratio of a multiple of the metrics to the resultant magnitude of the metrics; $(S*T)/(S^2+T^2)$ as well as the square roots of this value. These metric combinations are rough equivalents to a dot product between vectors. Many other combinations of metrics were evaluated and a majority of them showed similar trends.

Many of the metrics indicated that the horizontal 30/10 pattern produced the largest sensation of thermal perception while the lowest was generated by the diagonal 45/15 pattern. However, the metric combination that showed the most unique results was the ratio of temporal sensation metrics to spatial sensation metrics: T/S.

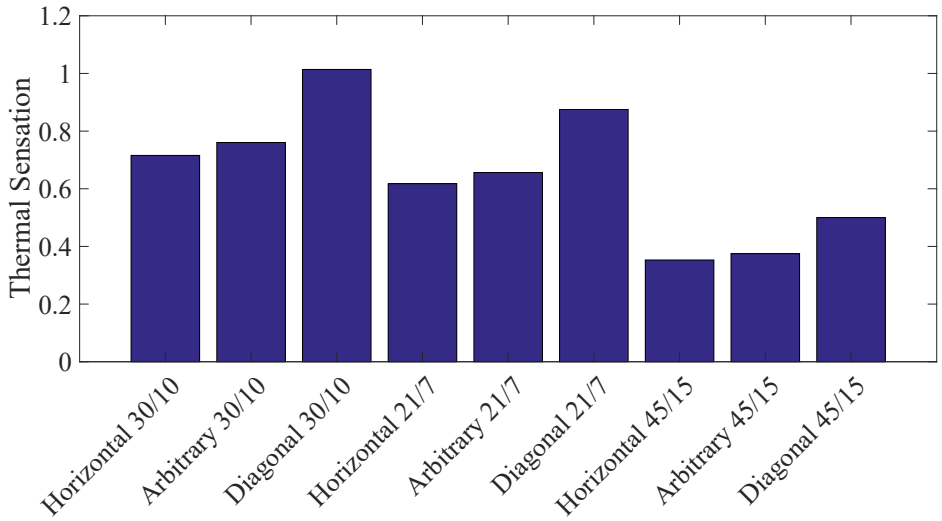

Figure 3.34: Combined temporal and spatial pattern metrics. The ratio of temporal to spatial pattern metrics is shown for each set of simulated patterns. This data is used as the primary correlation metric between thermal sensation and heat flux.

Figure 3.34 shows that a certain pattern emerges from the combination of metrics. For each combination of timing pattern, the diagonal pattern is the most strongly perceived. The 30/10 pattern generated the strongest sensation of cooling expect when comparing the horizontal 30/10 combination to the diagonal 21/7 combination. The 45/15 timing patterns generated the weakest sensation of cooling for all spatial patterns. The values for each pattern combination are: horizontal 30/10 at 0.72, arbitrary 30/10 at 0.76, diagonal 30/10 at 1.01, horizontal 21/7 at 0.62, arbitrary 21/7 at 0.66, diagonal 21/7 at 0.88, horizontal 45/15 at 0.35, arbitrary 45/15 at 0.38 and diagonal 45/15 at 0.50. The theoretical correlation between these thermal perception metrics and the heat flux generated by each pattern combination is developed and applied in the following sections.

3.5.2 Correlation with Heat Flux

The thermal perception values stated in the previous section, Figure 3.34, were used to develop the relationship between heat transfer and thermal perception. In order to generate a relationship, the absolute maximum heat flux difference for the heat flux probes discussed in Section 3.4.2 was determined for each combination of temporal and spatial patterns. The heat flux difference was calculated for all coordinate directions (x, y and z) and the total magnitude which is the resultant heat flux, independent of direction. The heat flux difference in the total magnitude value showed the strongest relationship with the actual thermal perception. Figure 3.35 shows the absolute maximum heat flux difference for the heat flux probes.

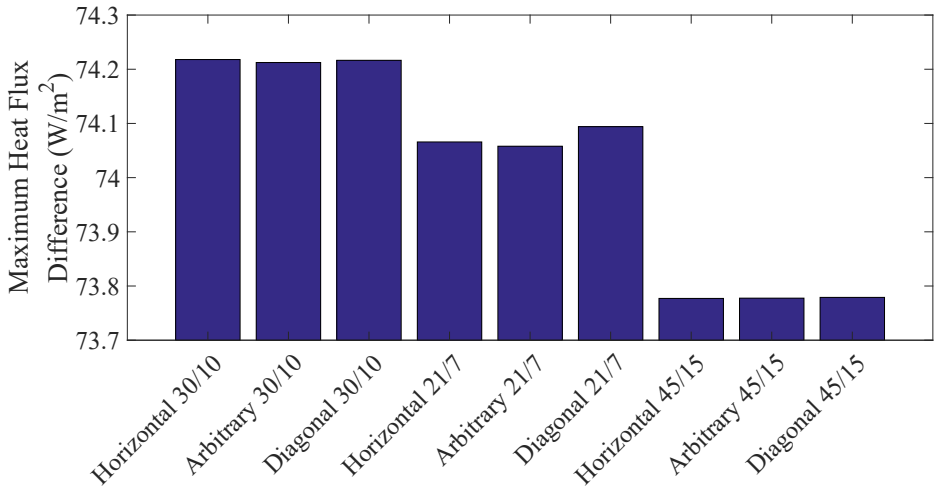

Figure 3.35: Absolute maximum heat flux difference for probes in the simulation. These heat flux differences for each combination of spatial and temporal patterns is shown. This information is used to generate a relationship between heat flux and thermal sensation.

A similar trend is seen when compared to Figure 3.34. The 31/10 and 21/7 heating/cooling patterns produce the largest heat flux difference values. The 45/15 pattern produces a noticeably smaller heat flux difference value. All of the heat flux difference values in Figure 3.35 were generated from the probe located directly under the second actuator. The area directly under and around the second actuator has consistently shown the largest heat flux difference values. Both

the thermal perception metrics and the absolute maximum heat flux difference values have shown similar trends. These two quantities are now plotted with perception as a function of heat flux.

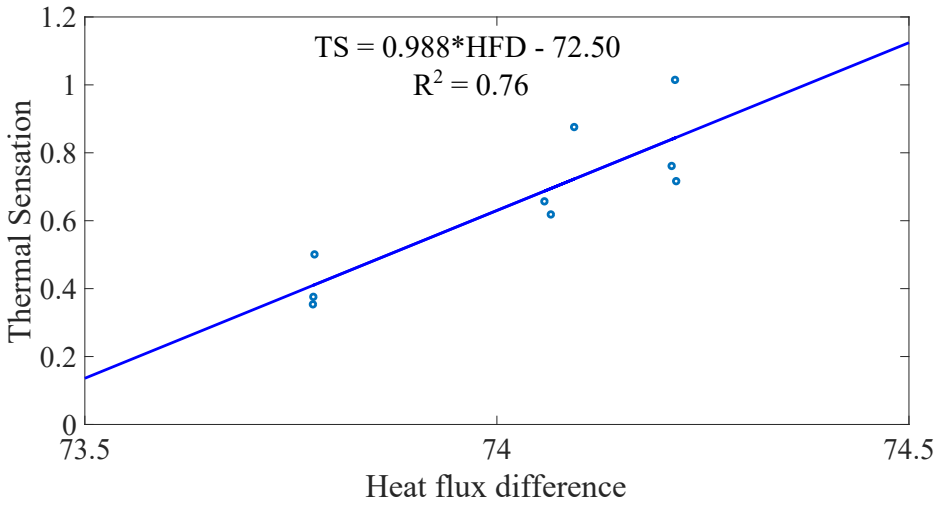

Figure 3.36: Mathematical relationship between thermal sensation and heat flux. The first approximation of a linear relation relation between actual thermal perception and heat flux is displayed. There is a 76 percent correlation between these two quantities. The data points in the plot are grouped by timing pattern. The first group of data points is 45/15 heating/cooling, the second group is 21/7 and the third group is 30/10.

Figure 3.36 expresses the relationship between thermal sensation (TS) and heat flux difference (HFD). This relationship shows an R^2 value of 0.76. Each group of three data points has timing pattern in common. This implies that the affects of temporal patterns have a stronger impact on thermal sensation. The thermal sensation averages for each group is 0.83 for 30/10, 0.72 for 21/7 and 0.41 for the 45/15 pattern. The thermal sensation standard deviations for each is 0.161 for 30/10, 0.139 for 21/7, and 0.08 for the 45/15 pattern.

$$TS = 0.988 * HFD - 72.50 \tag{3.8}$$

TS is the Thermal Sensation and HFD is the heat flux difference. The relationship described in Equation 3.8 shows a linear correlation between heat flux and thermal perception. This

relationship will now be used to determine the potential efficiency of newly developed temporal and spatial patterns.

3.6 Optimizing Heating and Cooling Patterns

The three linear heating/cooling time patterns that have been most heavily investigated include 21/7, 30/10 and 45/15. The analysis employed here was to take the take the difference between the global maximum and global minimum for each directional heat flux value for the first five probe locations between the first two actuators. The heat flux profile produced by each of these linear time patterns is similar, differing by between 4.05 percent and 20.06 percent at specific locations. Three primary spatial patterns were considered throughout this study: horizontal, diagonal and arbitrary. Again, the difference between the global maximum and global minimum for each directional heat flux value was taken and plotted with respect to probe location. The three patterns also produced very similar heat flux profiles, differing between 0.01 percent and 3.68 percent for some locations.

It is desirable to increase the effectiveness of the of the heating and cooling cycles in order to increase the sensation of constant cooling. Three methods are investigated with the intent of increasing the sensation of cooling: two different time patterns and one spatial pattern. The two time patterns to be examined are overlapping heating/cooling cycles and non-linear time patterns. The spatial pattern to be examined is a rearranged pattern. Additionally, these new patterns will be combined in order to observe the heat flux profiles produced by each.

3.6.1 Overlapping Time Patterns

The overlapping heating/cooling pattern is focused on overlapping the individual actuator segments. This pattern is such that the second actuator segment reaches its peak value before the first actuator segment reaches its lowest value. Under the standard pattern, the first actuator segment is at its initial value, 31.5°C, as the second actuator segment reaches its peak value, 32.5°C.

A way to achieve the overlapping pattern is to require the segment delay to be reduced from ten seconds in order for the peak values to overlap. Using the same 30/10 heating/cooling pattern, the smaller delay would cause a larger gap between the initial heating of the fourth actuator segment of the first cycle and the heating of the first actuator segment of the second cycle.

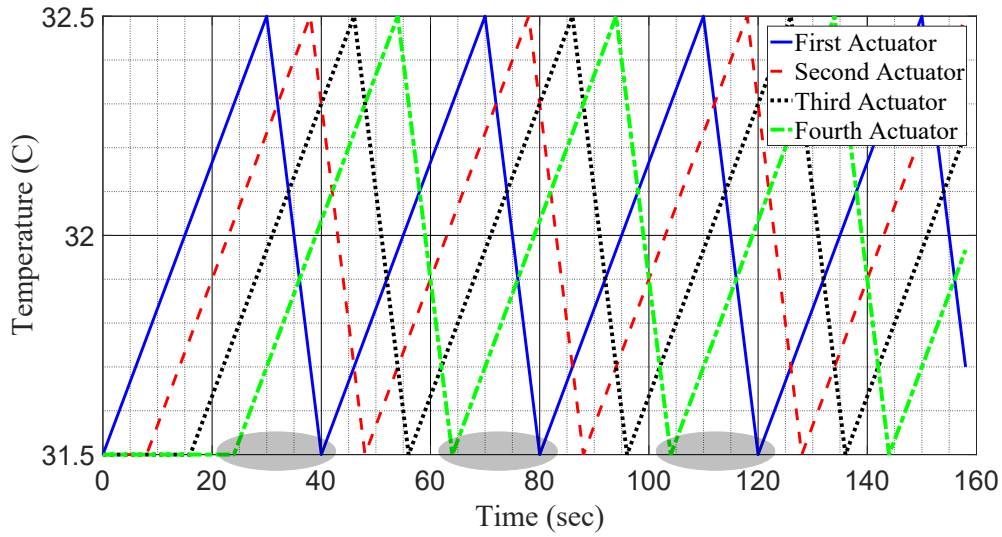

Figure 3.37: Incorrect overlapping temporal pattern. The circled sections indicate the excessive gap in the timing pattern generated by the 30/10 heating/cooling cycle with an eight second delay.

The timing pattern in Figure 3.37 shows the excess gap between the entire heating/cooling cycle produced by the standard 30/10 pattern with an eight second delay. This pattern is incorrect because it does not meet the requirement that three actuator segments are heating with one segment at its peak temperature,32.5°C, while one actuator segment is at its minimum temperature value, 31.5°C. This pattern could be corrected if an additional row of actuators was added to fill that excess space between heating actuators. However, for the current physical setup of four rows of actuators, a new timing pattern must be created.

To achieve the desired overlap of actuators and ensure that there is not an excess gap between actuator heating, the required time pattern becomes 28/12 heating/cooling with a ten second delay between actuators. This new time pattern yields the actuator temperature profile seen in Figure 3.38.

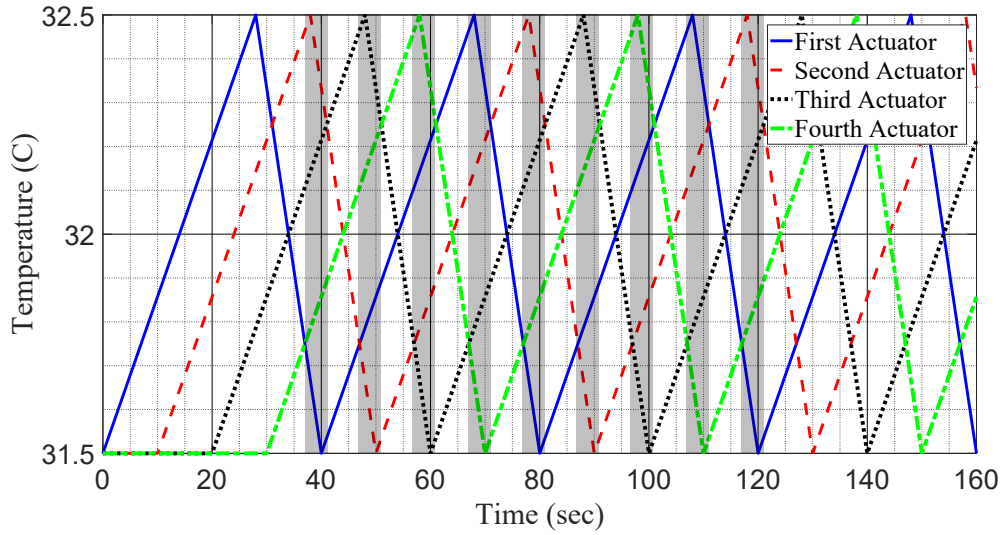

Figure 3.38: Proper overlapping temporal pattern. 28/12 heating/cooling pattern with ten second delay. This pattern allows the individual actuator segments to overlap properly. The highlighted section indicates the overlapping segment in which the total cooling area doubles for two seconds.

The 28/12 heating/cooling pattern in Figure 3.38 does not follow the three-to-one heating and cooling ratio of the standard timing patterns. This is a new timing pattern but it can also be seen as a new spatial pattern. This is because the location of heating and cooling actuators does not conform to the standard pattern one row at a global maximum, and one row at a global minimum. The new locations of actuators relative to these temperature extremes makes it an altered version of the three standard spatial patterns. It can be observed in Figure 3.38 that when one actuator is at its maximum temperature value, the adjacent actuator has not reached is minimum temperature value. For approximately two seconds the after an actuator reaches its peak value, two actuators are cooling at the same time. This means that the area of cooling has doubled for a specific amount of time. According to Kenshalo [5], the thermal threshold decreases as area increase, and since the perceptible threshold is already surpassed, this increased area will only make the thermal sensation more perceptible.

3.6.2 Rearranged Heating and Cooling Patterns

The rearranged pattern involves changing the locations of heating and cooling actuators relative to when a particular segment reaches its peak temperature (refer to Figure 3.22). To this point, all patterns have consisted of four actuator segments that alternate heating and cooling in a standard direction. That is, the first segment of actuators begins heating/cooling then the second, then third and fourth before the same cycle begins again. In all cases, there is a very clear, ordered, unidirectional pattern of heating and cooling of the actuators. This means that the temperature differential between neighboring actuators (in the z direction), is always the same for a given pattern.

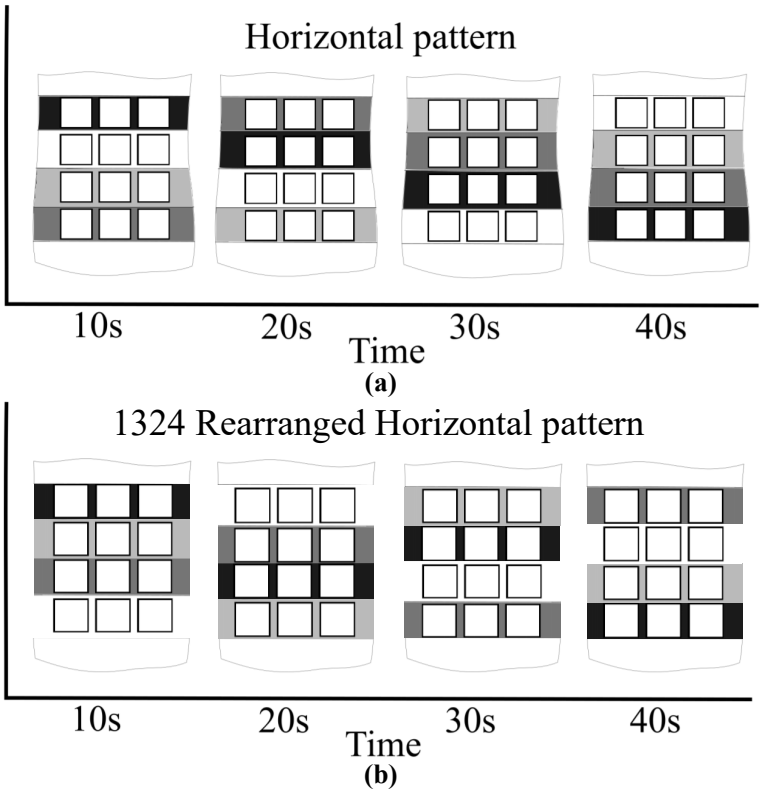

Figure 3.39: Comparison of horizontal and horizontal rearranged. (a) The standard horizontal pattern. 2016 IEEE (b) The rearranged horizontal pattern in the 1324 format.

Figure 3.39 shows the difference between standard and rearranged horizontal patterns. Rearranging the locations of the different actuator segments relative when they begin heating changes

the temperature differential between actuators. The idea for this type of pattern modification is that it may allow for more diffusion and storage of heat in both the positive and negative z direction. This means a larger and more evenly distributed area of skin may be subject to heated and cooled thermal energy and therefore may lead to increased thermal sensation. This is opposed to heat diffusion over a smaller area and avoids heating and cooling the same section between actuator segments consecutively. This would hold true for all patterns. Additionally, this will allow for increased examination of the directional dependence of thermal perception. Heat transfer will remain the same for the y direction. Now, however, due to changing temperature differentials between neighboring actuators heat transfer in the x and z direction will be different. The magnitudes of these changes is discussed in the following section.

3.6.3 Non-Linear Time Patterns

For this section of the study, the 30/10 heating/cooling pattern has been modified and applied to the three spatial patterns to see the effects of non-linear cooling. The non-linear timing pattern follows the standard three-to-one ratio. As with the standard patterns, the heating segment of the pattern is at the same rate as the linear pattern, 0.03 °C/s, which is below the rate for thermal perception. The cooling segment is where the non-linearity is examined. The cooling segment will still consist of decreasing one degree over ten seconds to maintain the three-to-one ratio. Figure 3.40 shows the non-linear heating/cooling pattern. The heating rate is standard. The cooling segment consists of a 0.75°C drop in temperature in two and a half seconds. This is followed by a 0.15°C drop in temperature over two and a half seconds and finally a 0.1°C drop in temperature for the last over the final five seconds.

The theory is that rapid cooling in the first two and a half seconds of the cooling segment will allow for more time at a lower temperature before heating begins again. Not only is the actuator cooling faster, the first time step of the cooling segment sees the actuator temperature fall below skin temperature. This will cause negative heat flow into the skin for a longer period of time and at a larger total magnitude. It is theorized that this pattern modification will produce the

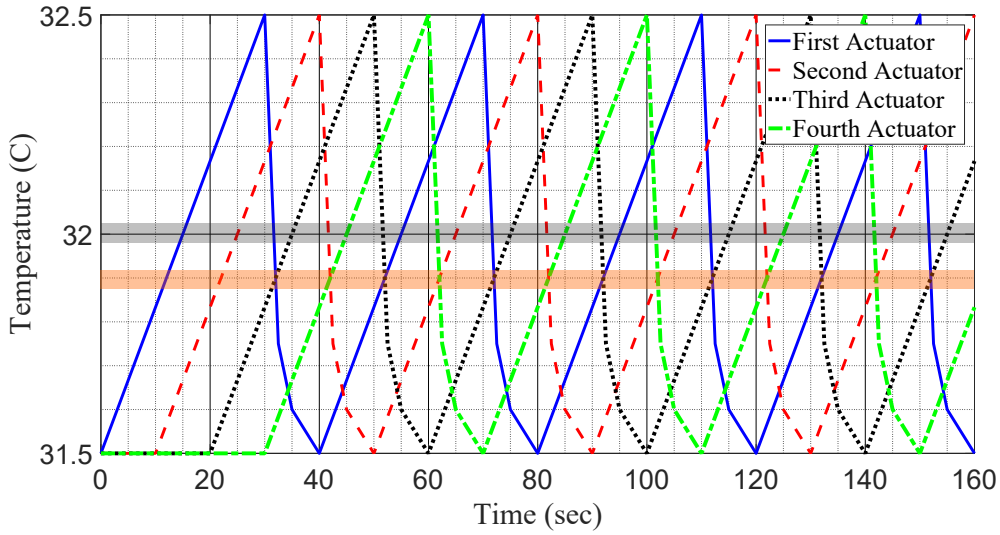

Figure 3.40: The 30/10 non-linear heating and cooling pattern. This pattern consists of the standard heating rate with rapid cooling in order to for the actuator be at a cooler temperature for longer. The red highlight indicates the desired average temperature, 32°C. The yellow highlight shows the average temperature produced by this pattern, 31.9°C.

strongest sensation of cooling of the three new patterns. In the current iteration of the non-linear time pattern, the average temperature is slightly shifted down to a value of approximately 31.9°C. This does not meet the requirement of the average skin temperature not being affected, however, the pattern will still be evaluated as a first approximation of non-linear effects of non-linear timming.

3.6.4 Efficiency of Optimized Patterns

The heat flow characteristics of the optimized patterns discussed in the previous section are evaluated and their increased or decreased efficiency in thermal perception is stated based on the theoretical correlation developed in Equation 3.8. The same method that was used to evaluate the nine standard patterns is used here. The five probe locations that were previously selected are chosen here for consistency in evaluation. The global maximum and global minimum values in heat flux, for all directions and the total magnitude, for each probe location is determined and the difference is taken. Again, this is referred to as the heat flux difference value. The heat flux probe

with the maximum total magnitude value for heat flux difference is determined and this value is used to determine the theoretical efficiency of thermal perception.

The overlapping 28/12 heating/cooling pattern with ten second initial delay was applied to all three spatial patterns: horizontal, arbitrary and diagonal. The overlapping pattern displayed some promising results. The heat flux difference values for the new pattern increased an average of 1.7 percent. The overlapping horizontal pattern produced a heat flux difference of 75.49 W/m^2 up from 74.22 W/m^2 for the standard horizontal pattern. The overlapping arbitrary pattern produced a heat flux difference of 75.47 W/m^2 up from 74.21 W/m^2. The overlapping diagonal pattern generated an HFD of 75.46 W/m^2 up from 74.22 W/m^2 for the standard diagonal pattern.

The heat flux difference values generated by the overlapping patterns produced a theoretical thermal sensation of approximately 2.1 for the diagonal pattern based on Equation 3.8. This is approximately double the thermal sensation as the diagonal 30/10 heating/cooling pattern. The theoretical thermal sensation for the horizontal and arbitrary increases by more than double. A possible explanation for this increase in thermal sensation could be the increased area of cooling at regular intervals over the course of the simulation. The area is effectively increased by a factor of two and therefore the thermal threshold is reduced. The horizontal pattern increase by approximately 190 percent from 0.72 to 2.1. The horizontal pattern has the largest continuous area of thermal actuation and therefore when the area of cooling doubles for a period of time, the thermal concentration is the largest. Its is possible that for the overlapping horizontal pattern, the cooling sensation generated by the actuators may appear to be moving. The reason for this hypothesis is that, with the periodically changing area of cooling, the location of more "intense" cooling will be changing. Lee et al. [44] showed that localization of cooling stimuli is much stronger that heating stimuli and with the altering location and area of the cooling stimuli the movement of cooling may be more strongly perceived

The rearranged pattern was applied to the three spatial patterns at the 30/10 heating/cooling rate. This was deemed appropriate for analysis because it has been shown that time scaling has a smaller effect on heat flux profile than changing the spatial pattern. This pattern modification

produced heat flux difference values than are approximately the same as the standard patterns. The heat flux difference values for the rearranged horizontal and diagonal patterns is 74.22 W/m^2. The arbitrary pattern was negligibly larger at 74.23 W/m^2.

The rearranged pattern generated a theoretic thermal sensation lower than any of the standard patterns. The rearranged horizontal and diagonal patterns both produced a theoretical thermal sensation of 0.84 while the arbitrary pattern generated a theoretical thermal sensation of 0.85. These values constitute a 17 percent increase in thermal sensation for the horizontal pattern compared with the standard pattern, up from 0.75. The rearranged diagonal pattern showed a 17 percent decrease in thermal sensation compared with the standard diagonal pattern, down from 1.01. The theoretical thermal sensation generated by the rearranged arbitrary pattern showed an increase of 12 percent, up from 0.76.

The non-linear timing pattern was applied to the three spatial patterns. The rapid cooling segment of the actuators was theorized to produce the strongest sensation of cooling due to more time spent at a lower temperature. The hypothesis was proven true when using the equation for theoretical thermal perception (Equation 3.8). The heat flux difference values were much larger than any of the standard patterns or the newly created patterns; approximately 14.2 percent larger than the standard patterns and approximately 12.5 percent compared to the overlapping pattern. The heat flux difference values produced by the non-linear pattern were 84.81 W/m^2 for the arbitrary and diagonal pattern and 84.79 W/m^2.

The theoretic thermal perception values generated by this pattern were much larger than expected. The horizontal pattern generated a theoretic thermal perception of 11.29 while the arbitrary and diagonal pattern produced a perception of approximately 11.31, less than a one percent difference. These values are roughly 14 times larger than the standard patterns, five times larger than the overlapping patterns and 13 times larger than the rearranged patterns. It is unlikely that the thermal perception, which is based on the ASHRAE Standard 55 model, are as large as the values indicate. This shows the limitations of the model developed in Equation 3.8. However, its does seem to indicate a stronger level of thermal sensation and the non-linear pattern should

be further investigated. A possible explanation for the strong thermal sensation is that this pattern fails one of the initial requirements of the system; that the average temperature of the skin does not change. Because of the rapid cooling, the average temperature of the pattern is actually ten percent lower than skin temperature. Methods for utilizing the non-linear pattern without violating this requirement are given in the conclusion.

Chapter 4: Conclusion and Future Work

The heat flux characteristics of asymmetrically heated and cooled thermal stimuli have been investigated. Primary contributions of this thesis include (1) the determination of heat flux values and patterns for different heating and cooling rates. (2) the heat flow patterns present in the thermal display developed by Manasrah et al. [8] have been determined and evaluated. (3) reasons for the effectiveness of different spatial and temporal pattern combinations have been given. (4) a mathematic relationship between heat flux and thermal perception has been hypothesized. (5) new and modified patterns have been developed and evaluated to determine their potential effectiveness in producing a cooling sensation.

Heat flux values present in the system range from approximately -75 W/m^2 to 75 W/m^2. These numbers were determined analytically and backed up by numerous simulations. It was shown that for all pattern combinations the heat flux profiles are nearly identical. Additionally, the timing patterns served only to scale the heat flux magnitudes; ten percent in one instance. A linear theoretic relationship was developed between the simulated heat flux values and the experimental thermal perception.

A series of questions were formulated in the introduction with the intention of evaluating the effectiveness and causes of thermal perception. This research sought to answer these questions as clearly as possible. There seems to be evidence that suggests the resultant magnitude of the directional heat fluxes at each probe location is the primary factor for thermal sensation. Section 3.5 determined a first approximation of this relationship that produced an R^2 value of 0.76. The data suggested that the rate of change in temperature was a primary factor in producing thermal sensation. The 30/10 heating/cooling rate produced the strongest sensation followed by the 21/7 pattern and the 45/15 pattern produced the weakest sensation. This is consistent with preliminary

findings. While the resultant magnitude of heat flux was ultimately used to determine a relationship, this magnitude value was heavily influenced by the heat flux values in the radial dimension (y-direction). This is not surprising due to the fact that the heating source is orthogonal to the medium being heated. Timing rate was the primary factor in differentiating among heat fluxes produced and therefore the effects of perimeter and area seem to be a weaker indicator of thermal sensation.

Future work may help to validate some of the claims made by this thesis as well as address additional questions not answered by this work. Questions such as at what heat flux values is thermal sensation actually triggered, and whether this sensation remains once triggered or if it gradually fades if not actively maintained. In order to answer these questions, additional experimentation is required. A suggested question for future human experiments is: Please indicate the precise time when cooling is felt. Additionally, a test in which heating/cooling is switched off at the moment of cooling sensation and the time it takes for the cooling sensation to fade completely is measured may indicate the persistence of the cooling effect.

Placing two actuators of different sizes at multiple distances apart and fluctuating temperature could lead to a better understanding of the directional effects of heating and cooling. Similar questions may be asked to determine the subjects' thermal sensation. Additionally, a thermal imaging camera could potentially be used to visualize the heat flow patterns produced.

New timing patterns may also be developed to increase the induced thermal sensation. The non-linear pattern showed the most promising results when the theoretical correlation was applied. It was observed that the average temperature for this pattern was shifted down by ten percent. Therefore, a non-linear heating segment may help to bring the average temperature to the correct value. The overlapping pattern also showed an increased thermal perception but there is potential for a non-fixed feeling of cooling because of the alternating areas and locations of cooling. Increasing the number of actuators on the thermal display may combat this potential issue. Future simulations may be undertaken with the increased number of actuators to evaluate the characteristics of overlapping heating/cooling segments.

List of References

[1] Th E Finger. Evolution of taste and solitary chemoreceptor cell systems. *Brain, Behavior and Evolution*, 50(4):234–243, 1997.

[2] Kenneth O Johnson. The roles and functions of cutaneous mechanoreceptors. *Current opinion in neurobiology*, 11(4):455–461, 2001.

[3] Raf J Schepers and Matthias Ringkamp. Thermoreceptors and thermosensitive afferents. *Neuroscience & Biobehavioral Reviews*, 34(2):177–184, 2010.

[4] Dan R Kenshalo, Charles E Holmes, and Paul B Wood. Warm and cool thresholds as a function of rate of stimulus temperature change. *Perception & Psychophysics*, 3(2):81–84, 1968.

[5] DR Kenshalo. Correlations of temperature sensitivity in man and monkey, a first approximation. *Sensory functions of the skin with special reference to man*, pages 305–330, 1976.

[6] H Hensel and RD Wurster. Static behaviour of cold receptors in the trigeminal area. *Pflügers Archiv*, 313(2):153–154, 1969.

[7] H Benzing, H Hensel, and R Wurster. Integrated static activity of lingual cold receptors. *Pflügers Archiv*, 311(1):50–54, 1969.

[8] Ahmad Manasrah, Nathan Crane, Rasim Guldiken, and Kyle B Reed. Perceived cooling using asymmetrically-applied hot and cold stimuli. *IEEE transactions on haptics*, 2016.

[9] Jean Baptiste Joseph Fourier. *The analytical theory of heat by Joseph Fourier ; translated, with notes, by Alexander Freeman ; edited for the Syndics of the University Press.* Cambridge [Eng.] :University Press,. http://www.biodiversitylibrary.org/bibliography/18544 — Translation of : Theorie analytique de la chaleur.

[10] David W Hahn and M Necati Ozisik. *Heat conduction*. John Wiley & Sons, 2012.

[11] Bengt Sundén. *Introduction to heat transfer*. WIT Press, 2012.

[12] LS Kowalczyk. Thermal conductivity and its variability with temperature and pressure. *Trans. Am. Soc. Mech. Engr*, 77:1021–35, 1955.

[13] A Cengel Yunus and A Boles Michael. *Thermodynamics: An engineering approach*. 2006.

[14] Thomas C Schelling. Dynamic models of segregation. *Journal of mathematical sociology*, 1(2):143–186, 1971.

[15] Christian P Robert. *Monte carlo methods*. Wiley Online Library, 2004.

[16] Eric Bonabeau. Agent-based modeling: Methods and techniques for simulating human systems. *Proceedings of the National Academy of Sciences*, 99(suppl 3):7280–7287, 2002.

[17] Charles M Macal and Michael J North. Tutorial on agent-based modeling and simulation. In *Proceedings of the 37th conference on Winter simulation*, pages 2–15. Winter Simulation Conference, 2005.

[18] Sankaran Mahadevan. Monte carlo simulation. *MECHANICAL ENGINEERING-NEW YORK AND BASEL-MARCEL DEKKER-*, pages 123–146, 1997.

[19] Christopher Z Mooney. *Monte carlo simulation*, volume 116. Sage Publications, 1997.

[20] Junuthula Narasimha Reddy. *An introduction to the finite element method*, volume 2. McGraw-Hill New York, 1993.

[21] Daryl L Logan. *A first course in the finite element method*. Cengage Learning, 2011.

[22] Il-hwan Seo, In-bok Lee, Oun-kyeong Moon, Se-woon Hong, Hyun-seob Hwang, Jessie P Bitog, Kyeong-seok Kwon, Zhangying Ye, and Jong-won Lee. Modelling of internal environmental conditions in a full-scale commercial pig house containing animals. *biosystems engineering*, 111(1):91–106, 2012.

[23] Patrick M Knupp. Achieving finite element mesh quality via optimization of the jacobian matrix norm and associated quantities. part iâĂŤa framework for surface mesh optimization. *International Journal for Numerical Methods in Engineering*, 48(3):401–420, 2000.

[24] ANSYS Inc. *ANSYS Mechanical APDL Modeling and Meshing Guide*, 2013.

[25] Ralf Diekmann, Robert Preis, Frank Schlimbach, and Chris Walshaw. Aspect ratio for mesh partitioning. In *European Conference on Parallel Processing*, pages 347–351. Springer, 1998.

[26] Nell B Dale, Chip Weems, John McCormick, and John W McCormick. *Programming and Problem Solving with ADA 95*. Jones & Bartlett Learning, 2000.

[27] Barry G Green. The effect of skin temperature on vibrotactile sensitivity. *Perception & Psychophysics*, 21(3):243–248, 1977.

[28] Hsin-Ni Ho and Lynette A Jones. Contribution of thermal cues to material discrimination and localization. *Attention, Perception, & Psychophysics*, 68(1):118–128, 2006.

[29] Hsin-Ni Ho and Lynette A Jones. Development and evaluation of a thermal display for material identification and discrimination. *ACM Transactions on Applied Perception (TAP)*, 4(2):13, 2007.

[30] Ken Parsons. *Human thermal environments: the effects of hot, moderate, and cold environments on human health, comfort, and performance*. Crc Press, 2014.

[31] Joseph C Stevens. Thermal sensibility. *The psychology of touch*, pages 61–90, 1991.

[32] Barry G Green. Temperature perception and nociception. *Journal of neurobiology*, 61(1):13–29, 2004.

[33] AD Craig and MC Bushnell. The thermal grill illusion: unmasking the burn of cold pain. *Science*, 265(5169):252–256, 1994.

[34] Didier Bouhassira, Delphine Kern, Jean Rouaud, Emilie Pelle-Lancien, and Françoise Morain. Investigation of the paradoxical painful sensation (‘illusion of pain’) produced by a thermal grill. *Pain*, 114(1):160–167, 2005.

[35] Dieter Jaeger and Ranu Jung. *Encyclopedia of Computational Neuroscience*. Springer Publishing Company, Incorporated, 2015.

[36] Kerry H Levin and Hans Lüders. *Comprehensive clinical neurophysiology*. Saunders, 2000.

[37] Donald D Price, Roland Staud, Michael E Robinson, Andre P Mauderli, Richard Cannon, and Charles J Vierck. Enhanced temporal summation of second pain and its central modulation in fibromyalgia patients. *Pain*, 99(1):49–59, 2002.

[38] Stefan Lautenbacher, Miriam Kunz, Peter Strate, Jesper Nielsen, and Lars Arendt-Nielsen. Age effects on pain thresholds, temporal summation and spatial summation of heat and pressure pain. *Pain*, 115(3):410–418, 2005.

[39] Saeed Moaveni. *Finite Element Analysis Theory and Application with ANSYS, 3/e*. Pearson Education India, 2008.

[40] Theodore L Bergman, Frank P Incropera, David P DeWitt, and Adrienne S Lavine. *Fundamentals of heat and mass transfer*. John Wiley & Sons, 2011.

[41] ASHRAE Standard. Standard 55-2004 – thermal environmental conditions for human occupancy. *ASHRAE Inc., Atlanta, GA*, 2004.

[42] Poul O Fanger et al. Thermal comfort. analysis and applications in environmental engineering. *Thermal comfort. Analysis and applications in environmental engineering.*, 1970.

[43] Povl Ove Fanger. Assessment of man's thermal comfort in practice. *British journal of industrial medicine*, 30(4):313–324, 1973.

[44] David K Lee, Sandra LB McGillis, and Joel D Greenspan. Somatotopic localization of thermal stimuli: I. a comparison of within-versus across-dermatomal separation of innocuous thermal stimuli. *Somatosensory & motor research*, 13(1):67–71, 1996.

Appendices

Appendix A: IEEE Copyright Permission

This copyright permission applies to Figures 3.23, 3.24, 3.25, 3.32, 3.33 and 3.39a.

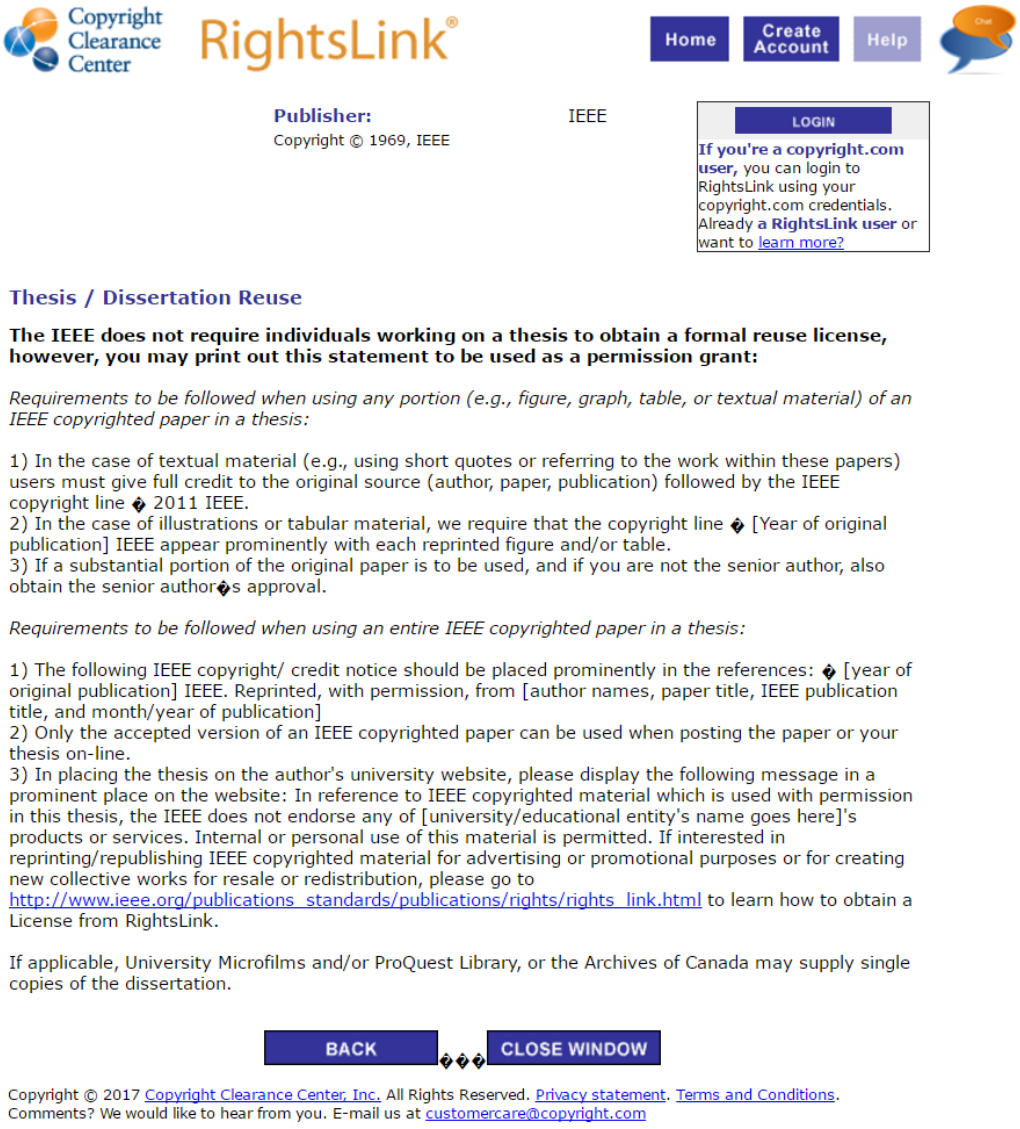

Copyright Clearance Center RightsLink®

Home | Create Account | Help

Publisher: IEEE
Copyright © 1969, IEEE

LOGIN
If you're a copyright.com user, you can login to RightsLink using your copyright.com credentials. Already **a RightsLink user** or want to learn more?

Thesis / Dissertation Reuse

The IEEE does not require individuals working on a thesis to obtain a formal reuse license, however, you may print out this statement to be used as a permission grant:

Requirements to be followed when using any portion (e.g., figure, graph, table, or textual material) of an IEEE copyrighted paper in a thesis:

1) In the case of textual material (e.g., using short quotes or referring to the work within these papers) users must give full credit to the original source (author, paper, publication) followed by the IEEE copyright line © 2011 IEEE.
2) In the case of illustrations or tabular material, we require that the copyright line © [Year of original publication] IEEE appear prominently with each reprinted figure and/or table.
3) If a substantial portion of the original paper is to be used, and if you are not the senior author, also obtain the senior author's approval.

Requirements to be followed when using an entire IEEE copyrighted paper in a thesis:

1) The following IEEE copyright/ credit notice should be placed prominently in the references: © [year of original publication] IEEE. Reprinted, with permission, from [author names, paper title, IEEE publication title, and month/year of publication]
2) Only the accepted version of an IEEE copyrighted paper can be used when posting the paper or your thesis on-line.
3) In placing the thesis on the author's university website, please display the following message in a prominent place on the website: In reference to IEEE copyrighted material which is used with permission in this thesis, the IEEE does not endorse any of [university/educational entity's name goes here]'s products or services. Internal or personal use of this material is permitted. If interested in reprinting/republishing IEEE copyrighted material for advertising or promotional purposes or for creating new collective works for resale or redistribution, please go to http://www.ieee.org/publications_standards/publications/rights/rights_link.html to learn how to obtain a License from RightsLink.

If applicable, University Microfilms and/or ProQuest Library, or the Archives of Canada may supply single copies of the dissertation.

BACK | CLOSE WINDOW

Appendix B: Element Quality Metrics for Cylinder

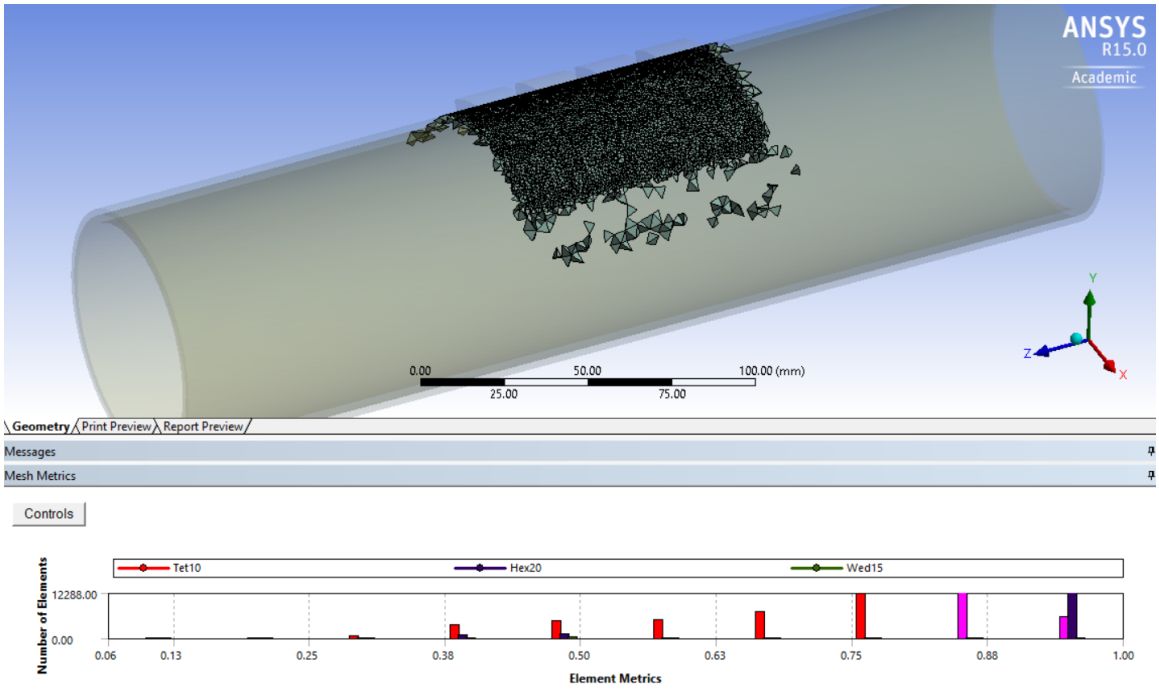

Figure B.1: Mesh quality on area of interest.

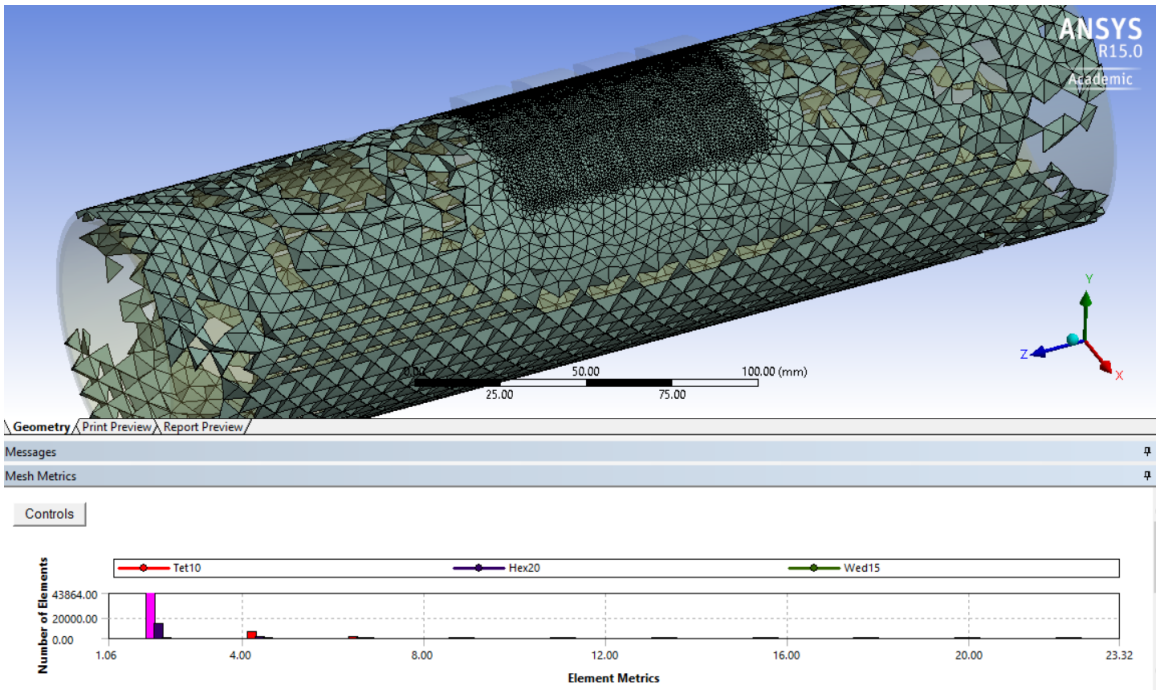

Figure B.2: Aspect ratio on area of interest.

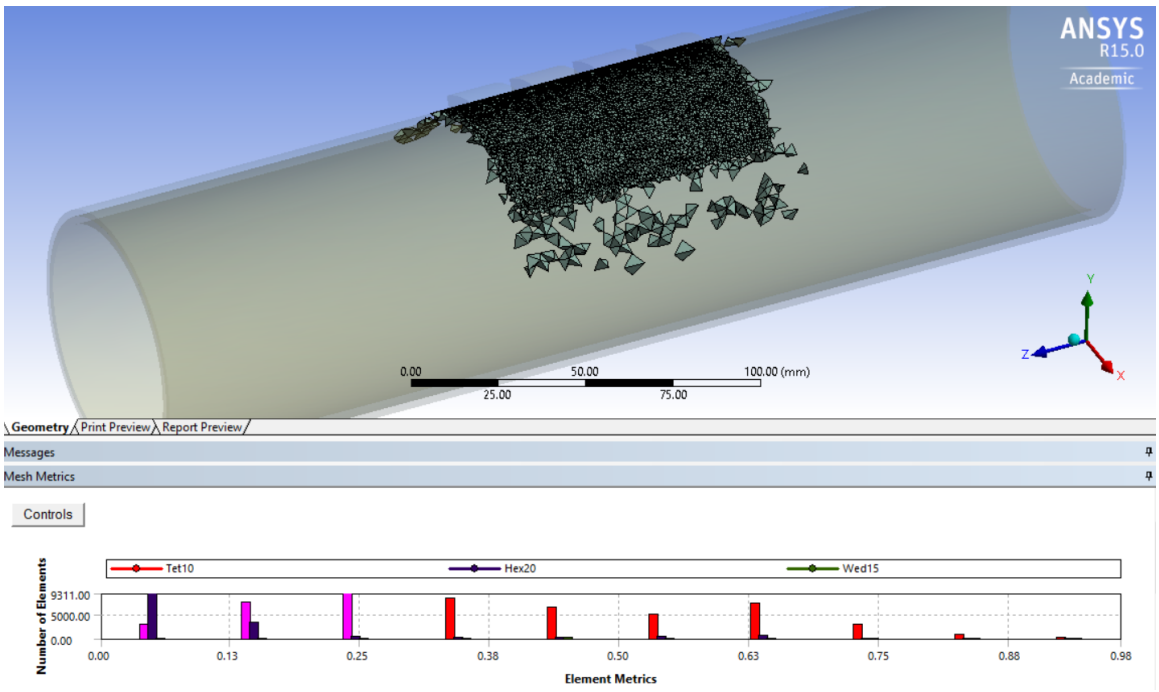

Figure B.3: Skewness on area of interest.